# Validation of UARS Microwave Limb Sounder temperature and pressure measurements

E.F. Fishbein[1], R.E. Cofield[1], L. Froidevaux[1], R.F. Jarnot[1], T. Lungu[1], W.G. Read[1], Z. Shippony[1], J.W. Waters[1], I.S. McDermid[1], T.J. McGee[2], U. Singh[3], M. Gross[3], A. Hauchecorne[4], P. Keckhut[4], M.E. Gelman[5], and R.M. Nagatani[5]

**Abstract.** The accuracy and precision of the Upper Atmosphere Research Satellite (UARS) Microwave Limb Sounder (MLS) atmospheric temperature and tangent-point pressure measurements are described. Temperatures and tangent-point pressure (atmospheric pressure at the tangent height of the field of view boresight) are retrieved from a 15-channel 63-GHz radiometer measuring $O_2$ microwave emissions from the stratosphere and mesosphere. The Version 3 data (first public release) contains scientifically useful temperatures from 22 to 0.46 hPa. Accuracy estimates are based on instrument performance, spectroscopic uncertainty and retrieval numerics, and range from 2.1 K at 22 hPa to 4.8 K at 0.46 hPa for temperature and from 200 m (equivalent log pressure) at 10 hPa to 300 m at 0.1 hPa. Temperature accuracy is limited mainly by uncertainty in instrument characterization, and tangent-point pressure accuracy is limited mainly by the accuracy of spectroscopic parameters. Precisions are around 1 K and 100 m. Comparisons are presented among temperatures from MLS, the National Meteorological Center (NMC) stratospheric analysis and lidar stations at Table Mountain, California, Observatory of Haute Provence (OHP), France, and Goddard Spaceflight Center, Maryland. MLS temperatures tend to be 1-2 K lower than NMC and lidar, but MLS is often 5 – 10 K lower than NMC in the winter at high latitudes, especially within the northern hemisphere vortex. Winter MLS and OHP (44°N) lidar temperatures generally agree and tend to be lower than NMC. Problems with Version 3 MLS temperatures and tangent-point pressures are identified, but the high precision of MLS radiances will allow improvements with better algorithms planned for the future.

## 1. Introduction

The Upper Atmosphere Research Satellite (UARS) reached Earth orbit on 12 September 1991 [*Reber*, 1993] carrying the Microwave Limb Sounder (MLS) and a suite of nine other instruments. MLS began limb scanning on 19 September 1991, has made near-continuous near-global measurements of temperature through Oc-

[1] Jet Propulsion Laboratory, California Institute of Technology, Pasadena, California.

[2] NASA Goddard Spaceflight Center, Greenbelt, Maryland.

[3] Hughes STX Corporation, Lanham, Maryland.

[4] Service d'Aeronomie du Centre National de la Recherche Scientifique, Verrieres le Buisson, France.

[5] Climate Prediction Center, National Centers for Environmental Protection, National Weather Service, NOAA, Camp Springs, Maryland.

tober 1994 and continues with near-global coverage to the present. MLS has generated one of the longest records of temperature profiles derived by limb sounding, and the precision and vertical resolution of these profiles are offering refined views of the thermal and dynamical state of the middle atmosphere [*Fishbein et al.*, 1993; *Randel et al.*, 1993; *Canziani et al.*, 1994; *Massie et al.*, 1994; *Ray et al.*, 1994].

Temperature and atmospheric pressure at the tangent point of the field of view boresight (hereafter called tangent-point pressure) are retrieved from the same set of measurements, and are validated together in this discussion. Pressure is the independent coordinate for all geophysical parameters retrieved from MLS (see *Froidevaux et al.*, [this issue] *Lahoz et al.*, [this issue] and *Waters et al.*, [this issue] for $O_3$, $H_2O$, and ClO validation, respectively), and tangent-point pressure inaccuracy and imprecision are contributors to their potential errors ("error" collectively refers to precision, accuracy, and stability, and all errors quoted will be $1\sigma$ bounds). We examine only the "Version 3" data and will use two validation approaches. In the first the error bud-

get is estimated by propagating parameter uncertainties through the retrieval algorithms. In the second, errors are obtained from comparisons with several correlative data sets. The advantage of the first method is that accuracies are independent of other data sets and are therefore not biased by potential inaccuracies in these data sets. However, since the MLS measurement system may be imperfectly characterized, comparisons with other data sets provide a consistency check and facilitate scientific analyses.

This paper begins with a description and characterization of the measurement system, which is composed of instrument and atmosphere models. Section 3 describes the data processing and retrieval algorithms, shows averaging kernels and parameter correlations, and gives examples of results. Section 4 shows examples of radiances and spectral signatures of model parameters and compares simulated and measured radiance residuals. Section 5 estimates the precision and accuracy of the temperature and tangent-point pressure based on the measurement model. Section 6 compares the MLS temperature fields to the U.S. National Meteorological Center (NMC) daily stratospheric analyses and lidar soundings. Section 7 compares the error estimates from section 5 to average differences with correlative data, and summarizes the estimates of accuracy and precision. Section 8 describes current and future work to improve the MLS temperature and tangent-point pressure measurements.

## 2. Description of the Measurement System

The measurement system is comprised of instrument and atmosphere models and its understanding is necessary for defining a set of error sources. The instrument model characterizes the relation between microwave thermal emissions from the atmosphere and output signal from the instrument (channel counts). The atmosphere model describes the generation of microwave thermal emissions and includes the representation of atmospheric structure, both vertical and horizontal, its composition, emission spectroscopy, and the radiative transfer calculations. Through a study of these two models, we arrive at a list of parameters whose errors are propagated through our analysis system to arrive at an error budget; a list of these parameters and their errors is contained in Table 1. The instrument model, which describes the conversion of measured signals to calibrated limb radiance is discussed by *Jarnot et al.* [this issue] (hereinafter referred to as J96), and the MLS forward model, which includes the atmosphere model, is described by Read et al.(manuscript in preparation, 1996; hereinafter referred to as R96).

### 2.1. Instrument Model

MLS measures millimeter wavelength thermal emission in spectral intervals near 63, 183, and 205 GHz. Temperature and tangent-point pressure are retrieved from 63-GHz radiances, emitted by molecular oxygen ($O_2$). This emission is due to transitions in which the combined spin of two unpaired electrons changes direction relative to the molecular rotation axis. These transitions have been used to remotely sense atmospheric temperature from space since the Nimbus E Microwave Spectrometer (NEMS) on the Nimbus 5 satellite [*Waters et al.*, 1975], and are currently used in the Microwave Sounder Units (MSU) on operational meteorological satellites [*Grody*, 1993].

**Table 1.** Precision, Accuracy, Bias and Stability of Measurement Model Parameters Divided into Instrumental and Atmospheric Sources

| Parameter | Precision | Accuracy | Bias | Stability | (Period) |
|---|---|---|---|---|---|
| **Instrumental** | | | | | |
| radiometric calibration | 0.03 – 0.33 K | 0.8% | | < 0.02% | (36 day) |
| antenna HPBW | | 3% | | < 0.03% | (36 day) |
| extraneous radiance | | 0.75 K | | 0.25 K | |
| sideband ratio | | 10% | | | |
| scan reference height | 800 m | 500 m | | 100 m | (36 d) |
| | | | | 600 m | (orbit) |
| **Atmospheric** | | | | | |
| $O_2$ line strength | | <0.1% | | | |
| $O_2$ line broadening | | 6% | + 6% | | |
| $^{18}OO$ line strength | | < 0.1% | | | |
| $^{18}OO$ line broadening | | 15% | | | |
| forward model | 1% | 1% | | | |
| Earth radius | 30 m | | | | |
| satellite altitude | 100 m | | | | |
| magnetic field | 0.02 G | | | | |
| $^{18}OO$ VMR | 300 ppmv | | | | |
| $O_2$ VMR | 300 ppmv | | | | |
| LOS velocity | 70 m/s | | | | |

The radiometric noise is listed in the precision column of radiometric calibration. Radiometric calibration accuracy and stability arise primarily from FOV related parameters. Magnetic field precision is for each component, and $O_2$ and $^{18}OO$ volume mixing ratios (VMR) precisions are height-independant upper bounds.

MLS has three radiometers, each based on a super-heterodyne receiver (see *Barath et al.* [ 1993] for an instrument description). For the purpose of parameterizing instrument response the instrument can be divided into three subsystems, the antenna, radiometers, and filter banks. The limb is scanned by the antenna, which focuses limb emission into the horns of the radiometers. Radiances measured by the 63-GHz radiometer are combined with a 63.283-GHz local oscillator signal by a double-sideband mixer, and upper and lower sideband signals are passed through two intermediate frequency single-sideband stages to a 15-channel, $\approx$500-MHz-wide filter bank. The 15 collective 63-GHz channels are referred to as "band 1," and are numbered 1–15. Channels have similar characteristics on each side of band center (e.g., channels 2 and 14) and are narrower toward the center; signal to noise is roughly proportional to the square root of the channel width.

The signal entering the radiometer contains radiances emitted by the limb of the Earth averaged over the antenna field of view (FOV), and a small "extraneous radiance" comprised of thermal emission from the instrument (mostly the antenna primary element), scattered radiances from the primary mirror's surface roughness, spillover of the primary past the secondary, and edge diffraction. The thermal component of the extraneous radiance is spectrally flat over the filter bank bandwidth and scan independent, but the scattered and diffracted components may be weakly scan angle dependent. The scaling of channel counts to brightness temperature is accomplished using space and calibration target views that are interspersed with the limb views by a switching mirror between the antenna and the radiometer. The brightness temperatures of the target (inferred from its measured emissivity and temperature) and space, along with prelaunch calibration measurements of the losses along optical paths, are incorporated in a linear model relating limb counts to limb radiance brightness temperature. The radiometric gain is the proportionality constant in this relation. Departures from the linear relation are estimated to be less than 0.1%.

Data are formatted in 65.536 s units called MLS major frames (MMAF), each having a unique index (`MMAF_-number`). MMAFs are further broken into 32 subunits called MLS minor frames (MMIFs), indexed from 1 to 32. A radiance measurement of either limb, calibration target, or space is made each MMIF. A limb scan is completed in one MMAF and is nominally composed of 26 limb views interspersed with six calibration measurements. A scan is discretely stepped from 90 to 0 km in tangent-point altitude and is adjusted for the Earth's oblateness and the orbit eccentricity to within 1.5 km (3.0 km prior to 8 April 1992). The average spacing between tangent-point altitudes is 6 km in the mesosphere, 3–4 km in the middle and upper stratosphere, and 1.5–2 km in the lower stratosphere and troposphere. Absolute altitudes are determined during processing from an encoder mounted on the antenna scan axis and UARS orbit/attitude knowledge. The accuracy of absolute altitudes is limited by UARS attitude knowledge and is around 1 km. Differences between tangent points are

known to around 80 m, of which 30 m arises from the encoder resolution. The discrete scan samples the limb slightly differently for each MMAF, differing only by an MMAF-dependent, MMIF-independent altitude offset (see Table 2 of J96 for tangent-point heights of the nominal scan). The altitude of a reference MMIF (MMIF 16) characterizes the overall positioning of the scan within the atmosphere, and is referred to as "scan reference altitude."

The orbit is inclined 57° to the equator, and the orbit plane precesses by 360° every 72 days. MLS samples the Earth's limb 90° from the flight direction on the shaded side of the satellite, along a minor circle (tangent track) offset approximately 23° (along the great circle) from the sub orbital track. The tangent track extends over a latitude range from 80° in one hemisphere to 34° in the other, and the hemisphere receiving maximum coverage reverses approximately every 36 days when UARS executes a 180° yaw maneuver. The time between yaw maneuvers is called a yaw period. Solar and measurement time are strongly correlated in this viewing geometry, and solar time, both at the MLS and the tangent-point, slowly precesses during a yaw period. Across a yaw maneuver, solar time at the tangent-point changes by more than 3 hours, shifting forward on one side of the orbit and backward on the other. On any day the ascending or descending side of the orbit (defined by whether latitude is increasing or decreasing with time) samples essentially the same local solar time at a given latitude.

Instrumental sources of error arise from uncertainty in the antenna FOV, the channel spectral responses, the radiometric gain, and the channel sideband ratios; errors in the modeling of the extraneous radiance and sampling error by the discrete scan. The antenna FOV and channel spectral responses are tabulated functions of angle and frequency. The half-power beam width (HPBW) and the radiance-weighted channel shape (described by J96) are parameters introduced to characterize these functions. For the purpose of propagating errors through the analysis system, the antenna pattern was stretched by a factor consistent with the uncertainty in the HPBW. Similarly, the channel spectral response was perturbed by a multiplicative slope consistent with the estimated uncertainty in the radiance-weighted channel shape. In determining which functional perturbations best characterize errors, several types of perturbations were applied to the FOV and channel spectral response, and these produce the largest changes to calculated radiances. The dominant source of error in the radiometric gain is associated with losses along optical paths and is expected to be channel and MMIF independent; measured radiances were rescaled by a channel-independent factor to study radiometric gain errors. The instrument model contains sideband ratios for each channel, but because errors in sideband ratio are expected to be highly correlated between adjacent channels, sideband ratio errors have been represented by a single channel-independent multiplicative factor. Instrumental errors also arise from the extraneous radiance, i.e., scattered and emitted radiance from the optical path. Sensitivity of temperature and

**Table 2.** Changes in MLS Instrument Operations Through 9 September 1993

| Date | Event |
|---|---|
| 19 Sept. 1991 | start of MLS observations |
| 17 Oct. 1991 | scan changed to improve sensitivity in the lower stratosphere |
| 31 Oct. 1991 | improved oblateness correction |
| 8 April 1992 | resolution of oblateness correction increased from 2.5 km to 1.25 km |
| 2 – 14 June 1992 | first solar array anomaly (SAA), MLS off |
| 14 – 20 June 1992 | first SAA, operations intermittent |
| 20 June – 4 July 1992 | first SAA, band 3 and 183-GHz radiometer off |
| 13 – 17 July 1992 | second SAA, MLS off |
| 25 Sept. 1992 | integration time decreased from 1.8 to 1.7s |
| 16 – 20 April 1993 | 183-GHz radiometer failure, MLS off |

tangent-point pressure to extraneous radiance was studied by applying channel and MMIF-independent radiance offsets to the measured radiances, and processing the perturbed radiances through the analysis system. The error analysis for the scan reference altitude is performed from synthetic radiances that have been generated for an ensemble of scans, which view the same atmospheric state and differ by a height-independent altitude offset.

Many parameters are influenced by insolation and are weakly time dependent. For these parameters the accuracy is the time-averaged or zero-frequency component of the parameter time series. The stability, or departure from its average value, is characterized by the power contained in the Fourier decomposition of the time variation. In most cases, the time-dependence is dominated by changes over a yaw period, and the stability listed in Table 1 is usually the deviation from the mean over a yaw period. Time series of engineering data (see J96) suggest that changes in instrument performance (e.g., radiometric scaling, spectral response, and 'extraneous radiance') during the first 2 years of operation are significantly less than 1%. However, changes in MLS operation, such as modifications to the instrument control program, or power interruptions, might have affected instrument behavior and are listed in Table 2. On timescales of a few MMAFs, measurement repeatability (precision) has contributions from radiance measurement noise and reference scan altitude variability. A radiance noise that is channel and radiance dependent is calculated for each measurement and ranges from $0.3\,\mathrm{K}$ in the center channels looking at $\approx 250\,\mathrm{K}$ to $0.03\,\mathrm{K}$ in the wing channels when looking at $2.7\,\mathrm{K}$ (space). Radiance noise is based on measured system noise temperature which has been stable. Reference scan altitude varies on timescales of an orbit and the yaw period; its stabilities over both periods are listed in Table 1.

### 2.2. The Atmosphere Model

Radiative transfer near 63-GHz is dominated by molecular absorption in local thermodynamic equilibrium throughout the stratosphere and lower mesosphere. The atmosphere model includes lines from all significant emitters; 34 $O_2$ lines, 100 $^{18}OO$ lines, 64 $^{17}OO$ lines, and 7 $H_2O$ lines. Within the filter bank spectral range, only two $O_2$ lines at 62.998 and 63.569 GHz and four $^{18}OO$ lines have significant spectral signatures. The two $O_2$ lines are the primary emitters, and magnetic line splitting of each into 93 and 105 Zeeman components, respectively, is included in the calculations. Spectroscopic line strengths and transition frequencies are obtained from the JPL catalog [Poynter and Pickett, 1985; Pickett et al., 1992], and $O_2$ line shape parameters for Version 3 processing are from Liebe [1991]. Later analyses [Liebe et al., 1992] indicate that these pressure-broadening coefficients are 6% too large. $H_2O$ line shape parameters are obtained from Rosenkranz [1988] and Rosenkranz and Staelin [1988] and $^{18}OO$ line shape parameters are estimated from $O_2$ parameters.

Calculated spectra for emission from isothermal atmospheres are shown in Figure 1. The emission is from ray trajectories with tangent-point pressures at 1, 10, and 22 hPa and atmospheric temperatures of 225, 245, and 265 K. The position of the two sidebands are shown so that line widths and filter bank bandwidths can be compared, but antenna FOV smearing is not included in the calculations. The radiometer is designed so that the $O_2$ lines are centered on channel 8 and fold on top of each other in the intermediate frequency spectrum. The two $O_2$ lines have approximately equal line strengths and widths and become optically thick (saturate) in each channel at approximately the same pressure. For tangent-point pressures above 0.1 hPa (meaning at higher altitudes or lower pressures), the emission is primarily in the middle three channels, and all channels saturate below 50 hPa.

The emission depends on temperature, pressure, volume mixing ratio, line of sight (LOS) velocity, and magnetic field. The latter two parameters shift or split the line proportional to velocity or field strength and are significant only in the three middle channels, 7, 8 and 9. Magnetic line splitting is estimated from the 1985 International Geomagnetic Reference Field [Barraclough, 1987] and the LOS velocity is approximately the component of the Earth rotation velocity along the LOS. The emission in optically thin channels depends only weakly on temperature because the temperature dependencies
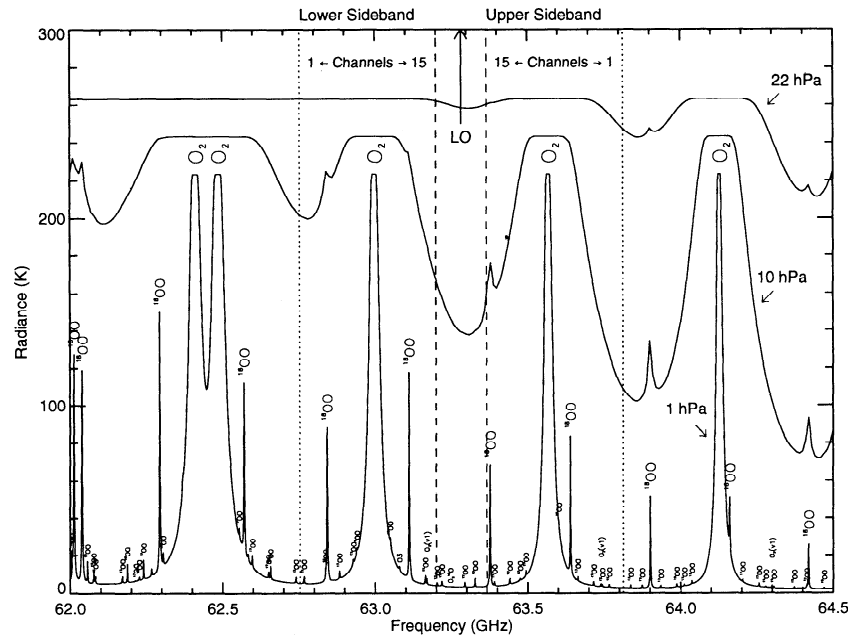
**Figure 1.** Synthetic spectra at 1 hPa, 10 hPa, and 22 hPa for isothermal atmospheres at temperatures of 225 K, 245 K, and 265 K, respectively.

of the line shape, line strength, and Planck function nearly cancel. Pressure sensitivity is strong whenever some channels are not saturated, and as seen in Figure 1, this occurs from 10 hPa to above 0.1 hPa.

The limb radiances entering the radiometer arrive from a range of tangent-point pressures determined by the tangent-point pressure at the boresight of the FOV, the antenna FOV shape, the distance to the limb and the temperature profile (vertical gradient of pressure) within the FOV. The dependence of the limb radiance on the pressure range over the FOV, which depends on temperature, accounts for approximately half the temperature sensitivity of unsaturated radiances and most of the sensitivity in the mesosphere.

Profiles of temperature, mixing ratio (VMR) and LOS velocity are represented as piecewise-linear functions in log pressure, with three evenly spaced breakpoints per decade of pressure (e.g., 10, 4.6, 2.2, and 1 hPa). Errors and perturbations in pressure will be reported in log-pressure coordinates $(H \ln P_0/P)$ where $H$ is the standard scale height (7 km) and $P_0$ is the reference pressure (1000 hPa); the vertical resolution of the representation basis is 5.4 km in these units. In Version 3 processing, along-track and LOS gradients are ignored within the volume viewed by a scan, so that temperature and mixing ratio fields depend only on pressure. Since for microwave emissions, radiance depends approximately linearly on temperature, errors from LOS gradients in microwave limb-sounding temperatures are smaller than those occurring in infrared limb-sounding temperatures.

## 3. Algorithms Producing Version 3 Data

The data are processed at the UARS Central Data Handling Facility (CDHF) in 24-hour segments, start-

ing with the first MMAF after 0000 UT. Raw MLS data are referred to as "Level 0". "Level 1" files contain calibrated radiances, antenna pointing, and engineering data. "Level 2" files contain the output from the retrievals, consisting of geophysical parameters and retrieval diagnostics. A further level of processing generates products on a common UARS grid, and these are referred to as "Level 3" files. Level 3 files are further categorized as Level 3A, containing profile data, and Level 3P, containing retrieval diagnostics and geophysical parameters other than profile data. Level 3A profiles are interpolated to a standard 43 level (indexed $0, \ldots, 42$) UARS grid that is evenly spaced in log pressure from 1000 hPa to 0.0001 hPa with six points per decade of pressure. The MLS retrieval grid is a subset of the UARS grid consisting of only the even UARS surfaces. Level 3A and 3P files are created on a time grid with profiles separated by 65.536-s intervals (L3AT and L3PT) or at 4° latitude intervals (L3AL and L3PL). The L3AT values on the even surfaces are the Level 2 retrieved profiles, while those on the odd surfaces are the averages of the adjacent surfaces. The Level 3AL profiles have an additional linear interpolation along the orbit track. The UARS gridding team (C. A. Reber and F. T. Huang, The UARS Level 3B gridding algorithm, manuscript in preparation) applies Kalman filtering to the Level 3AL data to generate a Level 3B product of zonal harmonics.

A version number is affixed to each file according to the processing stream that generated it. The Version 3 files have been generated for the entire mission to date. The format and contents of these files are described in the standard file description units (SFDU) documentation, available from the CDHF, NASA Goddard Space Flight Center.

The data processing stream has two stages. The

first generates calibrated radiances and radiance precisions and flags questionable data; the algorithms are described by J96. Geophysical parameters, Level 2, and Level 3 products are produced during the second stage; quality checking is done at both stages. For any MMAF, if either stage fails, the parameter MMAF_STAT contained in the Level 1 and Level 2 output files and in the Level 3P files is flagged as bad. Useful radiances and retrieved products are obtained from most limb scans, except for rare occasions, such as when the Moon appears in the FOV or the instrument experiences an anomaly (an error in the processing software improperly calibrated the radiances for ≈11 successive MMAFs on 6 October 1991, 2 February, 9 April and 11 September 1992, and 8 February and 11 March 1993. The retrieved parameters from these MMAFs are not valid, although Level 3 quality indicators do not flag the parameters as being bad).

### 3.1. Formulation of the Retrieval Algorithm

The retrieval algorithms are described by *Froidevaux et al.* [this issue] and are based on the sequential estimation technique described by *Rodgers* [1976]. The algorithm seeks to minimize residuals between a calculated radiance $y^c$ and the measured radiance $y$, weighted by an error covariance $E$. The retrieval solves the sequential estimation update equations

$$x_i = x_{i-1} + D_{i-1} \times (y_i - y^c{}_i) \qquad (1)$$

$$S_i = (I - D_i K_i) S_{i-1} \qquad (2)$$

$$D_i = S_{i-1} K_i^T \left( K_i S_{i-1} K_i^T + E_i \right)^{-1}, \qquad (3)$$

where $i$ is an index over the set of measurements, $x$ is the vector of retrieved parameters, and $S_i$ and $D_i$ are the solution covariance matrix and contribution functions after incorporating the $i$th measurement, respectively. The estimated uncertainties placed in the Level 2 and Level 3 files are the square root of the diagonal elements of the solution covariance matrix. The weighting functions $K_i$ have components $\partial y^c{}_i / \partial x$.

Radiances are assimilated starting at MMIF 1 and working sequentially downward, one MMIF at a time. The retrieved parameters for band 1 are the temperature profile above 46 hPa, the tangent-point pressures and the "baseline offsets." The 32 tangent-point pressures, and baseline offsets are MMIF dependent. Each baseline offset is a spectrally flat radiance, added to the calculated atmospheric radiance to account for the extraneous radiance described in the instrument model section. Unlike temperature, each tangent-point pressure and baseline offset coefficient affects radiances of the corresponding MMIF and is retrieved only from those radiance. Tangent-point pressures are retrieved only for MMIFs above 10 hPa. Below 10 hPa they are estimated, using hydrostatic balance, from the temperature profile at the start of the MMIF and the tangent-point pressure of the previous MMIF. At the end of the temperature retrieval the tangent point pressures be-

low 10 hPa are updated a second time using hydrostatic balance and the final estimated temperature; these updated tangent-point pressures are subsequently used in the constituent retrievals. Other parameters that weakly affect radiance, such as LOS velocity, temperature at 46 hPa and below, magnetic field, and the geocentric altitude of UARS and the tangent point, are 'constrained' to values appropriate for the MMAF being processed. The combination of retrieved and constrained parameters is called the "state vector."

The Version 3 retrieval algorithm employs a linearized forward model using table lookup to obtain radiances and their derivatives. The table is evaluated for a climatological atmosphere and is keyed by time (10 entries, one per UARS yaw period), latitude (8 bins, 20° wide centered on 70°S, 50°S, ..., 70°N), tangent-point pressure (43 interpolation points, 6 per decade of pressure from 1000 hPa to 0.0001 hPa), the sign of LOS velocity (i.e., whether the measurement is on the ascending or descending side of the orbit) and magnetic field strength (four bins). The tabulated values are interpolated to the estimated tangent-point pressures, using cubic splines for the radiances and linear interpolation for the derivatives, and uses the current estimated tangent-point pressure for each measurement. Therefore the model is nonlinear in tangent-point pressure. The magnetic field bins are keyed to field strength and have a fixed direction within each latitude bin; this representation is not sufficiently accurate for channels 7, 8, and 9, which consequently are not used in Version 3 processing.
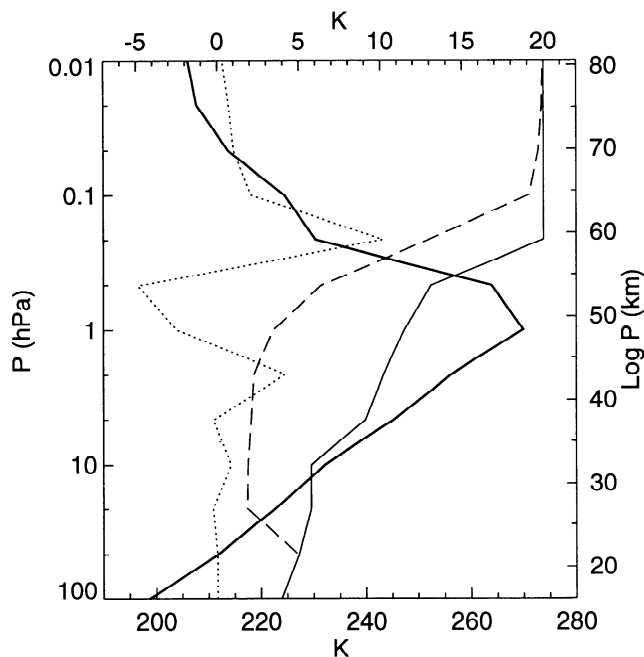
Error sources in the calculation of radiances arising from numerical approximations, "forward model noise", include nonlinear departures from the linearized forward model, quadrature error in integrals over frequency, ray path and antenna pattern, interpolation error associated with table lookups, and approximate representations of spectral line shapes of lines outside the filter bank bandpass. Based on sensitivity studies, linearization error dominates forward model noise and is less than 1% of the calculated radiance (R96).

The error covariance matrix $E$ is diagonal with each element equal to the square of the uncertainty in the difference between the estimated and the observed radiances. This uncertainty is equal to the root sum square (rss) of the measured radiance precision from Level 1 processing, the uncertainty in the estimated radiance arising from constrained parameters (the diagonal of $K_c S_c K_c^T$, where $K_c$ and $S_c$ are the weighting functions and the error covariance matrix for constrained parameters, respectively), an estimate of uncertainty in the forward model equal to 1% of the estimated radiance, and an error from the uncertainty in the scattering component of the extraneous radiation equal to 0.75 K. The terms in this sum are referred to as the "radiance measurement covariance," $E_m$, the "constrained parameter error covariance," $E_c$, the "forward model error-covariance," $E_f$, and the "extraneous radiance error-covariance", $E_s$. The diagonal elements of $S_c$, with the exception of temperature at and below 46 hPa,
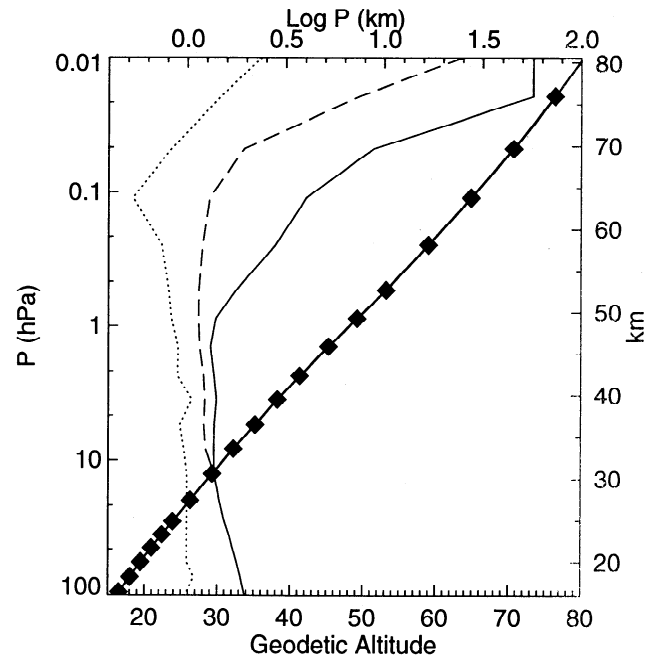
are the squares of the estimated precisions from Table 1; the temperature elements are the squares of the a priori errors described in the next section. The extraneous radiance error-covariance is an estimate of its channel-dependent component (assumed to be zero in the forward model) based on an examination of radiance residuals in outer channels when viewing the mesosphere. The forward model error-covariance is an estimate of the accuracy of the radiance calculations.

## 3.2. Formulation of the a Priori State

One profile is retrieved from each limb scan, starting with the state vector and its covariance set to an a priori estimate and its covariance. The a priori estimate for temperature is a linear combination of the UARS climatology and the NMC temperatures weighted inversely by their error covariances. The UARS temperature climatology is month and latitude dependent and is described by *Fleming et al.* [1988]. We use an uncertainty of 20 K for the UARS temperature climatology and an NMC temperature uncertainty equal to twice that estimated by NMC. NMC errors depend on height and location at 10 hPa and below, but only on height above 10 hPa, and are derived from comparisons with radiosondes and rocketsondes [*Schmidlin*, 1984]. The a priori tangent-point pressure is the tangent-point pressure of the previous tangent point plus the hydrostatic pressure difference using the temperature profile at the start of the MMIF. If the tangent-point pressure is not available from the previous MMIF, then the



**Figure 3.** Same as Figure 2 but for tangent-point pressure. The profile is plotted against the geodetic altitude, with the diamonds indicating the position of the tangent points. The units of the uncertainties and profile differences are height-equivalent log pressure, as defined in the text.

tangent-point pressure is evaluated using the mean scale height and the altitude of the 100-hPa surface (either from NMC or climatology). The a priori tangent-point pressure error-covariance is obtained by propagating the errors through the hydrostatic relation using uncertainties in temperature, altitude, and reference pressure; cross correlations between a priori tangent-point pressures are not included in Version 3 processing.

## 3.3. Case Study of a Retrieved Profile

We study here the profile derived from radiances of MMAF_number 579488, which occurred on 17 September 1992 at 10.0°N, 104.6°E, 0839 UT, ≈1000 km north of Singapore. The retrieved temperature profile and its uncertainties are shown in Figure 2. Also shown are the a priori uncertainties and the difference between the retrieved and the a priori profiles. The estimated uncertainties are relatively constant from 22 hPa to 1 hPa even though the a priori uncertainty increases uniformly. This indicates that the estimated uncertainty is dominated by the measurement error covariance. The error ratio, defined as the estimated uncertainty divided by the a priori uncertainty, measures the contribution of MLS information to the estimate and is less than 0.5 when MLS provides more than 75% of the information; this occurs from 22 to 0.46 hPa. The retrieved profile differs most from the a priori profile above 4.6 hPa, and since the a priori temperature below 0.2 hPa is primarily NMC temperature, this may indicate qualitative differences in how MLS and NMC



**Figure 2.** Retrieved profile (thick solid line), a priori uncertainty (solid line), estimated uncertainty from Version 3 processing (dashed line), and difference between a priori and retrieved profiles (dotted line) for temperature retrieval for MMAF 579488 (10.07° N, 105.6° E, 17 September 1992, 0839 UT). The lower scale is for the retrieved profile, while the upper scale applies to the remaining curves.

view the atmosphere. This will be discussed further in section 6.

Figure 3 shows the retrieved tangent-point pressure, the estimated uncertainties at the beginning and end of each MMIF, and the difference between the estimated and the a priori tangent-point pressure. Above 10 hPa the retrieved tangent-point pressure is the estimated tangent-point pressure after the last radiance for that MMIF has been assimilated into the retrieval, while below 10 hPa, tangent-point pressure is not retrieved directly from the radiances but is evaluated using hydrostatic balance with the retrieved temperature profile after the last radiance has been assimilated. Below 1 hPa the uncertainty is not significantly decreased by assimilating radiances from the current MMIF; tangent-point pressure is determined primarily from the tangent-point pressure of the previous MMIF and the pressure difference between MMIFs. Between 0.046 hPa and 1 hPa, tangent-point pressure is determined primarily by the radiances of the current MMIF, as indicated by the

large change in uncertainty before and after assimilating these radiances. Above 0.022 hPa the radiances are not sensitive to tangent-point pressure, and the estimate is primarily the a priori.

### 3.4. Characterization of the Retrieval

The model resolution matrix ($A = DK$) characterizes the sensitivity of the measurement system [*Rodgers*, 1990]. Rows of $A$ are the averaging kernels that characterize smoothing of the true state, while columns are the response of the vector of retrieved parameters to a unit perturbation of each individual parameter. Optimally, averaging kernels are $\delta$ functions, and departures from $\delta$ functions show how perturbations in the atmospheric state are misrepresented in the retrieved state. Plate 1 shows the model resolution matrix for Version 3 temperature, tangent-point pressure, and baseline offset. The measurements are sensitive to temperature perturbations from 22 hPa to 1 hPa but are noticeably degraded at 0.46 hPa and have little sensi-
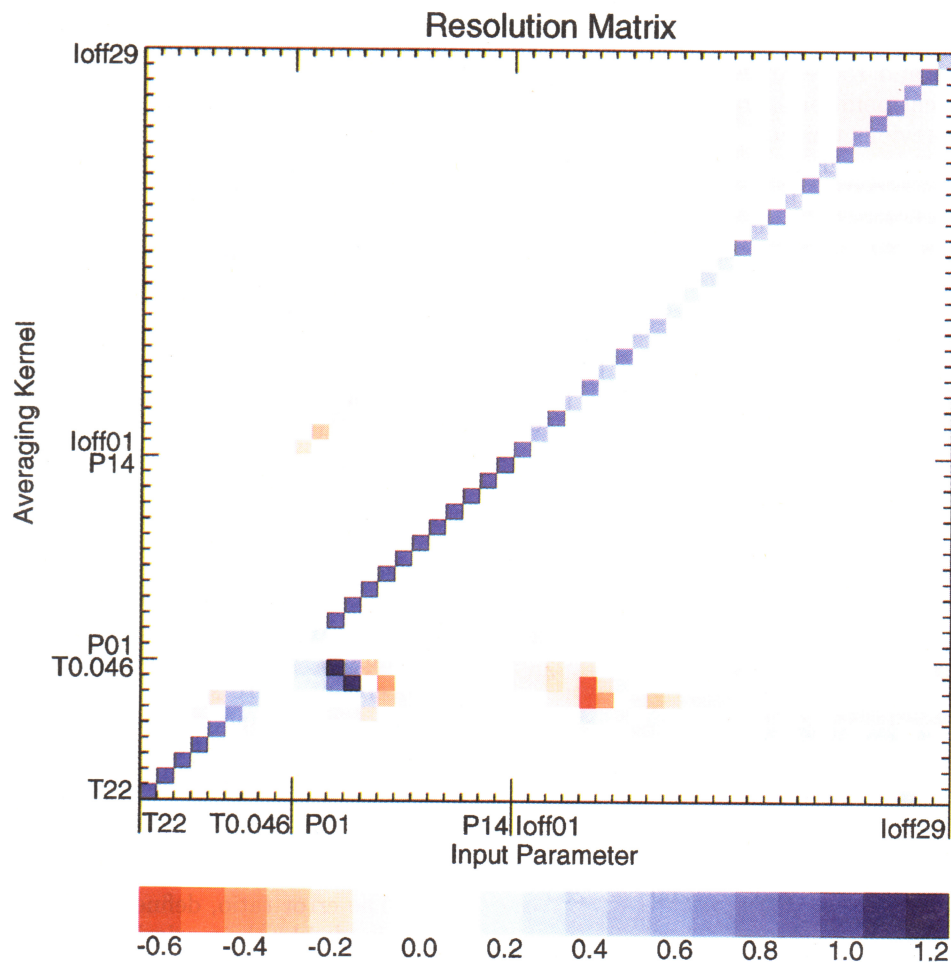


**Plate 1.** Model resolution matrix for the profiles shown in Figures 2 and 3. The averaging kernels are the rows of the matrix, showing smoothing of the true state (abscissa) in the estimated state (ordinate). The axis coordinates are the parameter names, 22 hPa temperature (T22) to 0.046 hPa temperature (T0.046); tangent-point pressure (P01, ..., P14) for thirteen MMIFs, 1 – 14, excluding 8, (P01, ..., P14); and 26 baseline offsets (Ioff01, ..., Ioff29), for MMIFs 1 through 29, excluding 8, 16, and 24. MMIFs 8, 16, 24, and 30 through 32 are used for calibration. Tangent-point pressure for MMIFs greater than 14 are below 10 hPa and are not retrieved for this MMAF.
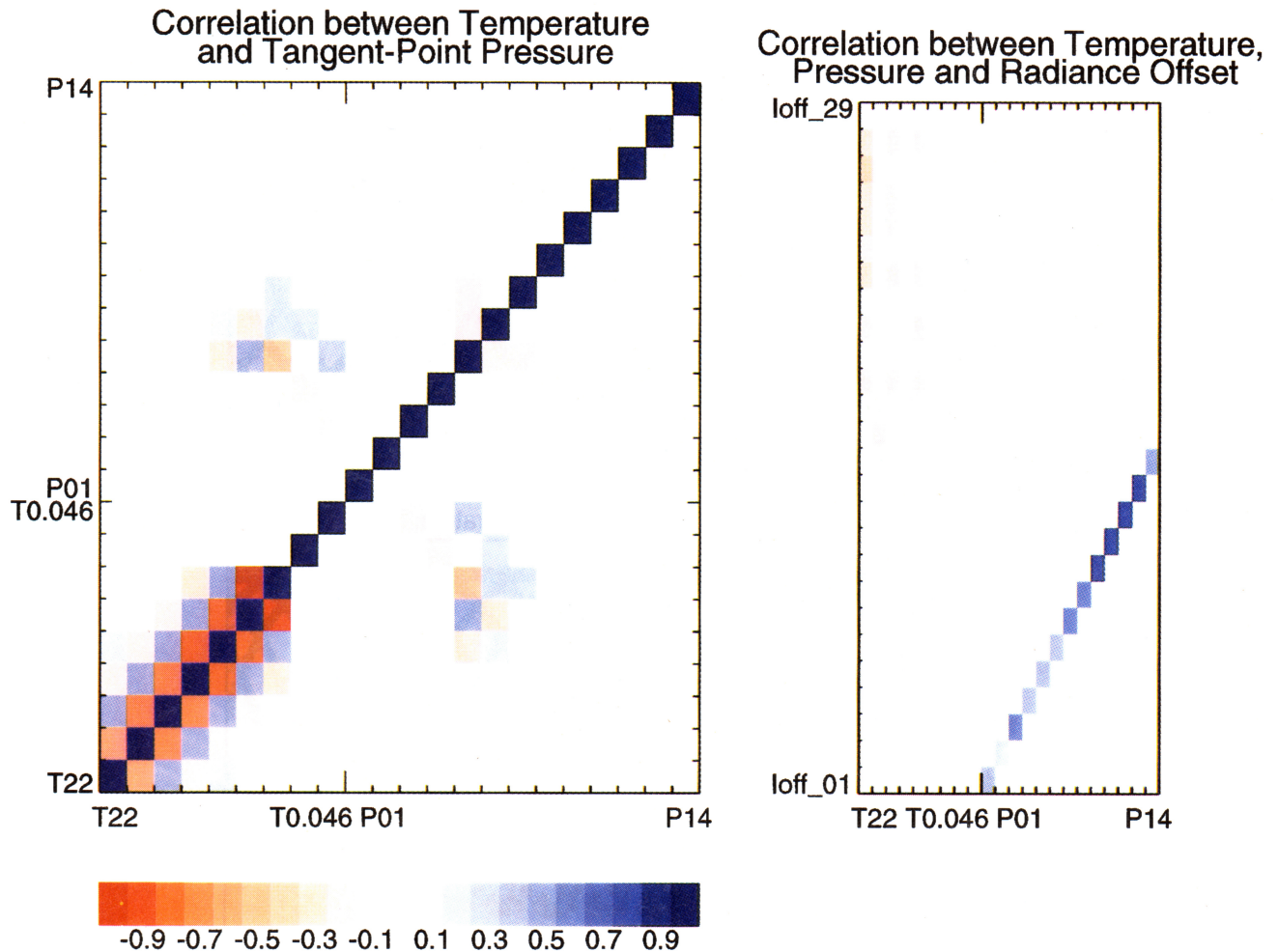
**Plate 2.** Correlation matrix for the same profile as in Figures 2, 3, and 1.

tivity to temperature above 0.46 hPa. The sensitivity to tangent-point pressure is good for MMIF 3 through MMIF 14 (the last MMIF above 10 hPa), but some of the tangent-pressure signal contaminates temperature coefficients above 0.46 hPa. MMIFs 1 and 2 have almost no sensitivity to tangent-point pressure, and the tangent-point pressure signal contaminates the baseline offset and temperature coefficients above 0.1 hPa. MLS 63-GHz radiances have the least sensitivity to baseline offset; several of the diagonal elements of the matrix are smaller than 0.7, and the contamination of temperature by baseline offset (off-diagonal coefficients in the model resolution matrix) is as large as 0.7 for temperatures above 0.46 hPa. Therefore a baseline offset of 1 K is expected to produce errors of around 0.7 K in temperatures above 0.46 hPa. Baseline offset affects temperature below 0.46 hPa by less than 0.2 K. Based on the averaging kernels, useful temperatures are provided by the MLS measurements between 22 hPa and 0.46 hPa, and useful tangent-point pressure can be retrieved between 10 hPa and 0.1 hPa.

Temperature, tangent-point pressure, and baseline offset are retrieved from the same radiances, so random uncorrelated errors in radiance can lead to correlated errors in the retrievals of these parameters. Corre-

lations between estimated temperature, tangent-point pressure, and baseline offset errors are characterized by a correlation matrix ($r_{ij} = S_{ij}/\sqrt{S_{ii}S_{jj}}$), shown graphically in Plate 2. The strongest correlations are between the adjacent temperature coefficients (always negative) and baseline offset and tangent-point pressure lower in the scan. The correlation length of the temperature profile errors is approximately 10 km in the mesosphere and decreases to 7.5 km in the midstratosphere; this is consistent with the HPBW of the antenna.

### 3.5. Retrieval Quality Indicators

The estimated uncertainties contained in the Levels 2 and 3 files (referred to **Profile_Sdev** in the SFDU documentation) on the even UARS pressure surfaces are the square roots of the diagonal elements of the estimated covariance matrix, while the estimated uncertainties in the Level 3 files on the odd surfaces are averages of the estimated uncertainties on the adjacent surfaces. When the error ratio is less than 0.5, the quality indicator is set negative to flag situations where the a priori estimate is weighted into the retrieval by more than 25%.

The quality indicators from a range of atmospheric conditions are now examined to address how quality varies with instrument performance and state of the
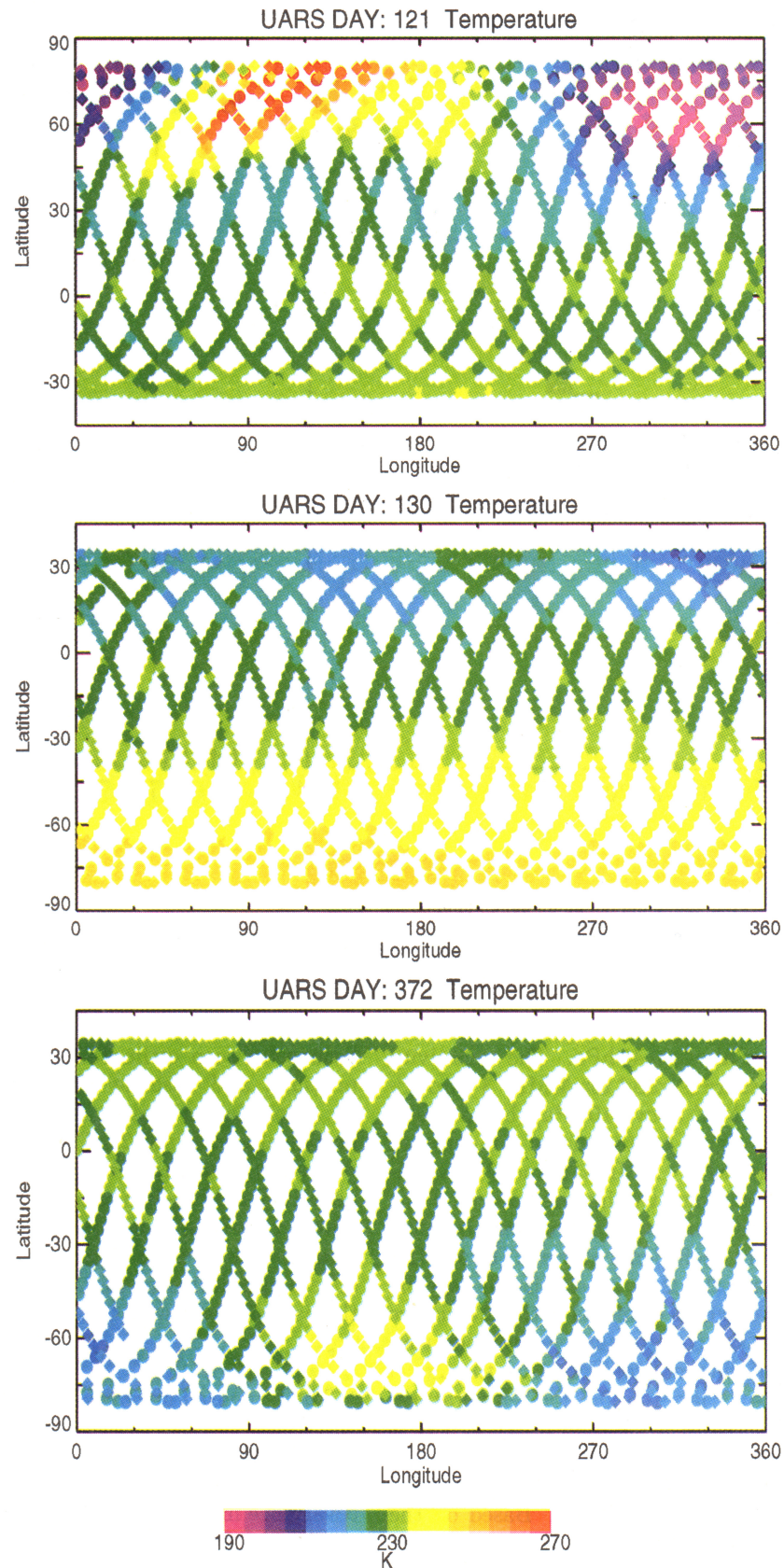
**Plate 3.** Retrieved temperatures at 10 hPa are shown for (top) 10 January 1992, northern winter; (middle) 19 January 1992, southern summer; and (bottom) 17 September 1992, southern winter. Solid circles are from limb scans on the ascending side of the orbit, diamonds are from descending side of the orbit. The solar times at the equator on the ascending/descending sides of the orbit are 22.7 hours/14.4 hours, 7.7 hours/23.4 hours, and 15.1 hours/23.4 hours for each day.

atmosphere. Plate 3 shows maps of estimated 10 hPa temperature on 10, 19 January, and 17 September 1992 (northern winter, southern summer, and southern late-winter). The greatest variability is seen in the map on 10 January 1992, where temperature variations are greater than 80 K, primarily at high latitude. The other maps show more modest variations, less than 20 K and primarily depending on latitude. Large variations in temperature over small changes in latitude are expected to produce the greatest errors arising from the latitude-dependent linearization of the radiance model, but errors associated with the spatial representation of the atmosphere (e.g., LOS and along-track gradients) are also expected to have an effect here. Accordingly, the quality of the retrieved temperatures should be poorest on 10 January. Near-colocated profiles are retrieved twice daily, approximately 12 hours apart from alternate sides of the orbit (ascending or descending latitude), and the estimated temperatures at the crossings agree to better than 5 K (the interval between colors), except during winter at high latitudes. The larger differences between colocated measurements are probably not associated with increased error since these error sources would be the same for either measurement but are probably associated with propagating atmospheric disturbances changing the state of the atmosphere during the 12 hours between measurements.

The estimated uncertainty of 10 hPa temperature is shown in Plate 4, and varies by less than 0.3 K root mean square (rms) over the globe. On 10 January 1992, 10 hPa estimated temperature uncertainty shows the greatest variability, mostly at high latitudes, and is weakly correlated with temperature. The estimated uncertainties depend on the weighting functions and the error covariance $\boldsymbol{E}$, which depends on the MLS scan, the linearization temperature profile, the radiances, and the radiance precisions. The linearization temperature profile depends only on latitude, and the radiance precision is nominally constant. Of the quantities affecting estimated uncertainty, variations in radiance and reference scan altitude are expected to produce the variations in uncertainty seen in Plate 4.

The estimated uncertainties do not depend on the level of closure between measured and estimated radiances; therefore profiles derived from radiances not accurately modeled can have small estimated uncertainties, even though the profiles themselves have poor quality. To address the issue of radiance closure, $\chi^2$ is provided as a diagnostic in the Level 2 output files; $\chi^2$ is defined as

$$\chi^2 = \frac{1}{N} \sum_i \frac{(y_i - y^c{}_i)^2}{\epsilon_i^2} \qquad (4)$$

where $N$ is the number of degrees of freedom, nominally 244 (the number of radiances minus the number of retrieved parameters for each MMAF) and $\epsilon_i$ is the radiance residual error. The radiance residual error is an independent estimate of the variance of the radiance residual distribution and for a perfect measurement model equals the radiance precision. The radiance residual error is an accurate estimate of the variance of the radiance residual distribution when $\chi^2$ is around 1. Typically, $\chi^2$ is around 200 for a radiance residual error equal to the radiance precision (used in Version 3 processing); this implies that radiance precision is not a good estimate of the variability of the residuals.

Maps of $\chi^2$ are shown in Plate 5 for the same days as in Plates 3 and 4. Errors in the measurement model are expected to be uncorrelated with radiance measurement precision, and residuals in the wing channel, which have the lowest noise, dominate $\chi^2$. The wing channels are most sensitive to temperatures at 10 hPa and 22 hPa, and therefore correlations between atmospheric structure and $\chi^2$ should be most significant at these levels; $\chi^2$ varies by more than a factor of 5 over the map (considerably more than the estimated uncertainty) and shows some correlations with atmospheric structure. Variations in estimated uncertainty are generally weak and unrelated to $\chi^2$; therefore estimated uncertainty is probably not a useful indicator of quality. High values of $\chi^2$ are correlated with warm temperatures at high latitudes during winter (e.g., on 10 January, north of 60°N near 30°E and on 17 September south of 70°S near 150°E) but are not correlated with high temperatures in summer high latitudes on 19 January.

The radiance residuals most likely arise from errors in the measurement model such as numerical approximations in the radiance calculations (e.g., model linearization), inaccuracy in instrument model or spectroscopic parameters, coarseness in the spatial representation of the atmosphere (e.g., LOS and along-track gradients), or an overly constraining a priori state. Residuals associated with errors in the instrument model or spectroscopic parameters are not expected to be spatially correlated and will be discussed in the following section. Concerning errors associated with model linearization, for the January anomaly, the linearization state temperature at 10 hPa north of 60°N is 203 K, which is approximately 60 K colder than the warmest retrieved temperatures, and for September the corresponding linearization temperature of 228 K is approximately 15 K colder. So linearization errors could be one source of large residuals. However, both regions of elevated $\chi^2$ are not centered on the warmest temperatures but are located more closely to where horizontal temperature gradients are largest (especially on 10 January). Residuals associated with the spatial representation are expected to be largest at high latitude during the winter, and the largest $\chi^2$ values are where the LOS is directed along the horizontal temperature gradient. However, differences between the estimated and the linearization temperature are largest here, and nonlinearity is also expected to be large. Finally, the atmosphere changes rapidly in this region during this period, and since the a priori temperature is primarily the daily NMC analysis, differences between the estimated and the a priori state are large.

The correlation matrix among $\chi^2$, LOS temperature gradient, difference between estimated and linearization temperatures, and difference between estimated and a priori temperatures provides some indication of the relative importance of these error sources. Using profiles from 10 January where $\chi^2$ is greater than 250, the matrix

$$\begin{matrix} 1.00 & 0.75 & 0.57 & 0.48 \\ 0.75 & 1.00 & 0.37 & 0.41 \\ 0.57 & 0.37 & 1.00 & 0.06 \\ 0.48 & 0.41 & 0.06 & 1.00 \end{matrix}$$

shows the correlations at 10 hPa among (from left to right, top to bottom) (1) $\chi^2$, (2) the LOS temperature gradient squared (evaluated from NMC temperatures), (3) the squared difference between estimated and linearization temperatures, and (4) the squared difference between estimated and NMC temperatures. The strongest correlations are between $\chi^2$ and the LOS temperature gradient; and the weakest are between the two temperature differences and between the LOS temperature gradient and the temperature differences. The weak correlation between LOS gradients and temperature differences means that correlations with $\chi^2$ and the other three fields are largely independent. The strongest correlation suggests that LOS gradients are a likely source of high $\chi^2$, and nonlinearity and a priori constraints are also potential sources, although weaker.

Plate 6 shows the time series of zonally averaged $\chi^2$ during the first 2 years of MLS operation; $\chi^2$ is generally between 100 and 200 at all times and has its smallest values near the equator and in the summer hemisphere. At these locations the thermal state of the atmosphere is weakly time dependent and homogeneous, and radiance residuals arising because the retrieval is over constrained to the a priori, the radiance model linearization is a poor approximation, or the spatial representation of the atmosphere is too coarse, are expected to be smallest. There is a tendency for $\chi^2$ to be smaller in the middle of yaw periods and this indicates that the stability of the measurement model varies with the yaw cycle. Zonal averages of winter high-latitude $\chi^2$ vary rapidly on timescales of a few days, and fluctuations are probably associated with polar vortex variability. Higher $\chi^2$ at winter high latitudes are probably associated with errors in the measurement model and suggest that temperatures during these times and locations may be of a poorer quality. Variations in estimated uncertainty (cf. Plate 4) are sometimes associated with variations in $\chi^2$, but in general, estimated uncertainty is not a reliable indicator of quality. Lastly, while $\chi^2$ is a measure of closure between measured and modeled radiances, its relation to retrieved temperature quality or uncertainty is not evident.

### 3.6. Retrieval Simulation Results

Retrievals from radiances generated from a model atmosphere, where the 'true' state of the atmosphere is known, provide a useful tool for analyzing error sources in the measurement system. In a typical observation mode, MLS is 'flown' over the model atmosphere and profiles of temperature and tangent-point pressure are sampled from the model along the MLS tangent track using simulated scan sequences; a random measurement noise is added for estimating precision. These synthetic measurements are processed through the processing software to generate estimated parameters; average and rms differences from model parameters provide estimates of retrieval biases and errors. The forward model used to generate the synthetic radiances has not been linearized, and any retrieval errors introduced from Version 3 processing forward model linearization are present in the simulated results. In addition, errors arising from the a priori state and smoothing in the averaging kernels are captured in the simulations, but errors in the measurement model arising from spatial resolution, spectroscopy, and instrumental model are not.

The model atmosphere used in this simulation is the retrieved state for 27 September 1992, and smoothed above 0.4 hPa to reduce noise. The temperature field at 10 hPa is equivalent to the temperatures shown in Plate 3. Temperature errors resulting from the retrieval are shown in Plate 7. The errors are on average less than 1 K, although differences are strongly correlated with location, such as the 2-3 K positive bias near 55°S, 315°E; $\chi^2$, also shown in Plate 7, is usually less than 5 and has larger values near 80°S, 175°E like the actual 27 September 1992 data.

The factor of 60 difference in $\chi^2$ between real and simulated data provides strong evidence that an error in the measurement model is responsible for the large $\chi^2$ values; $\chi^2$ is considerably larger at high latitude and is somewhat correlated with temperature uncertainty. This is probably resulting either from nonlinearity or from biases from the a priori, since LOS gradients are not present in the simulation. In section 6, MLS temperatures are shown to be ≈2 K colder than NMC temperatures in the midstratosphere. Since the model atmosphere is the MLS estimated field, it also is colder than the a priori state, and it is likely that the positive bias at 10 hPa is coming from the a priori state.

Figure 4 shows profiles of global averages of the difference between the estimated and model temperatures, rms estimated uncertainties, and the rms differences for the simulation. Biases and accuracies in the estimated temperature arising from the retrieval algorithm (i.e., sources other than errors in the measurement model) are estimated by the average and rms differences. The averaging kernels (Plate 1) show that MLS measurements are sensitive to temperature between 22 and 0.46 hPa, and within this range, rms differences are generally less than 1 K and the average differences are less than 0.5 K. Temperature at 0.46 hPa has significantly poorer agreement, mostly in the form of a negative bias; the averaging kernels indicate that MLS has less sensitivity here than between 1 and 22 hPa. The estimated uncertainty is considerably larger than the rms difference in the simulations and arises because the error covariance includes error sources attributed to the measurement model that are absent in the simulation.
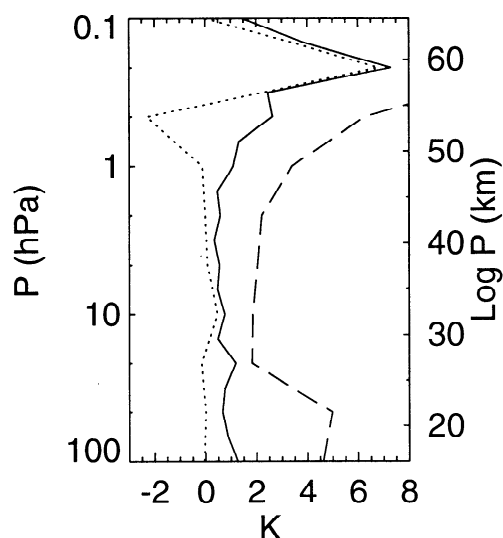
**Figure 4.** Global average of temperature uncertainty (dotted line), RMS difference (solid line), and RMS estimated uncertainty (dashed line) for simulations.

## 4. Radiances

In this section the radiances, the residuals between measured and calculated radiances, and the radiance weighting functions are examined to address why $\chi^2$ associated with retrievals from measured radiances are significantly larger than those from simulation. Simulated radiances and their radiance residuals from retrievals are shown in the first subsection. The second subsection describes a similar treatment for measured radiances and shows that the spectral signatures in the radiance residuals are not duplicated in the simulation. The third subsection presents the spectral signatures of retrieved parameters and shows that the differences in measured and simulated radiance residuals cannot be represented as sums of the spectral signatures of retrieved parameters. In the final subsection the spectral signatures of some measurement system parameters are shown, and potentially inaccurate ones are identified.
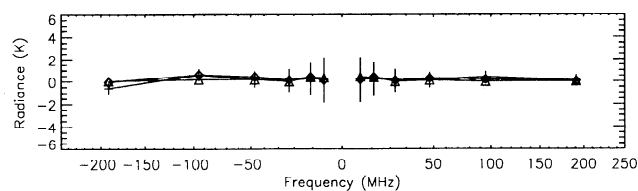
### 4.1. Residuals From Simulation

The quality of an individual retrieval and the significance of the radiance precision can be addressed by
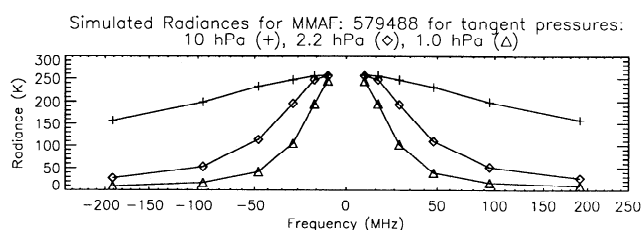


**Figure 5.** Simulated radiances for the reference scan interpolated to 10 hPa (pluses), 2.2 hPa (diamonds), and 1 hPa (triangles). Frequency along abscissa is relative to band center and is stretched toward band center to separate center channels. Plotting symbols indicate the centers of the channels (7, 8, 9 are not shown).
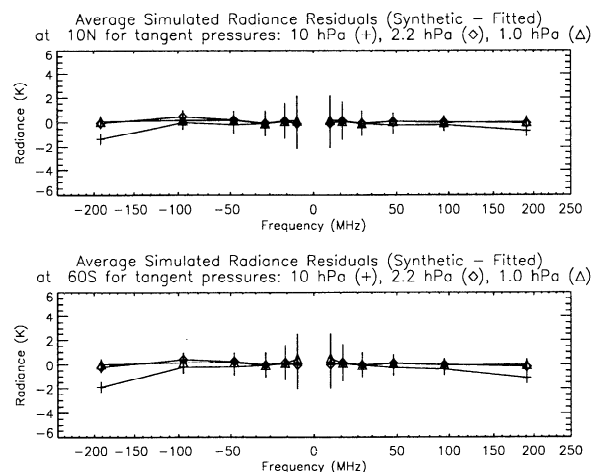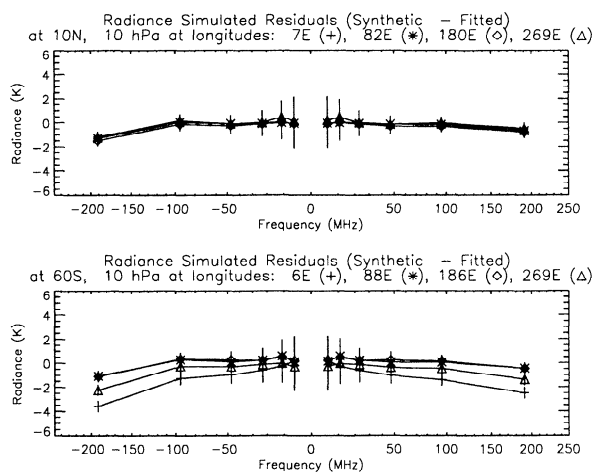


**Figure 6.** Radiance residuals from the simulated reference scan, interpolated to 10 hPa (pluses), 2.2 hPa (diamonds), and 1 hPa (triangles).

examining the radiances from a single scan, in this case the scan examined in the previous section (MMAF_number 579488). The radiances, interpolated to 1, 2, and 10 hPa, are shown in Figure 5. The radiances are approximately symmetric around the line centers and the asymmetry between corresponding channels (e.g., 1 and 15, 2 and 14) arises from $^{18}OO$ lines and atmospheric lines outside the filter bank bandpass. Figure 6 shows the radiance residuals and precisions for the same scan. The residuals are symmetric around band center and have discernible spectral signatures. Channels 6 and 10 saturate around 1 hPa and therefore the residuals in these channels are approximately independent of tangent-point pressure below 1 hPa. The wing channels have significantly better precisions, yet residuals have comparable amplitudes in all channels. Therefore even in simulation, radiance noise is much smaller than the residuals.

The spatial distribution of $\chi^2$ shows strong spatial correlations, and the next group of figures shows which radiances are primarily responsible for large residuals. The radiances are interpolated to evenly spaced log tangent-point pressures and latitudes along the orbit track to generate 'L3AL' radiances, and residuals are calculated from these gridded fields. Zonal averages are shown in Figure 7 at 10°N and 60°S. The largest residuals at 10 hPa occur in the wing and centermost



**Figure 7.** Zonally averaged radiance residuals derived from simulated radiances and interpolated along the scan track to the 10° N and 60° S parallels and to 10 hPa (pluses), 2.2 hPa (diamonds), and 1 hPa (triangles).

Radiance Simulated Residuals (Synthetic – Fitted)
at 10N, 10 hPa at longitudes: 7E (+), 82E (*), 180E (◇), 269E (△)

Radiance Simulated Residuals (Synthetic – Fitted)
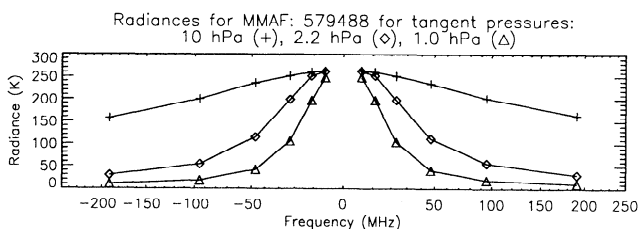at 60S, 10 hPa at longitudes: 6E (+), 88E (*), 186E (◇), 269E (△)

**Figure 8.** Radiance residuals from simulated radiances along the 10° N and 60° S parallel at 10 hPa. Residuals at 10° N are where the scan track crosses the parallels at 7° E (pluses), 82° E (asterisks), 180° E (diamonds) and 269° E (triangles). At 70° S, residuals are at 6° E (pluses), 88° E (asterisks), 186° E (diamonds), and 269° E (triangles).

Radiances Residuals for MMAF: 579488 for tangent pressures:
10 hPa (+), 2.2 hPa (◇), 1.0 hPa (△)

**Figure 10.** Same as Figure 6 but for measured radiances.

Average Radiance Residuals (Measured – Fitted)
at 10N for tangent pressures: 10 hPa (+), 2.2 hPa (◇), 1.0 hPa (△)

Average Radiance Residuals (Measured – Fitted)
at 60S for tangent pressures: 10 hPa (+), 2.2 hPa (◇), 1.0 hPa (△)

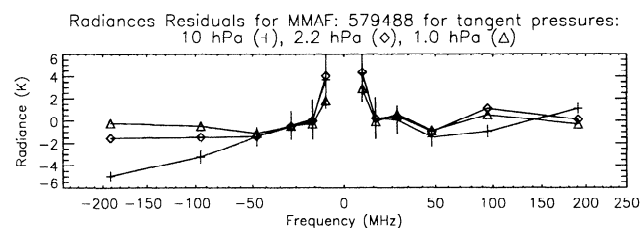**Figure 11.** Same as Figure 7 but for measured radiances.

channels and are larger for the high-latitude scans; $\chi^2$ is particularly sensitive to residuals in the wing channels which have the best precision, and variations in $\chi^2$ are primarily due to variations in radiance residuals in the middle and lower stratosphere in the outermost channels. Figure 8 shows a selection of radiance residuals at 10 hPa along the 10°N and 60°S parallels. While most of the residuals are 1 K or less, large residuals occasionally occur at high latitude (such as at 60°S, 180°E) and explain most of the variation in the zonal mean. In summary, large variations in $\chi^2$ are primarily indicative of lack of radiance closure in the wing channels toward the bottom of the retrieval range.
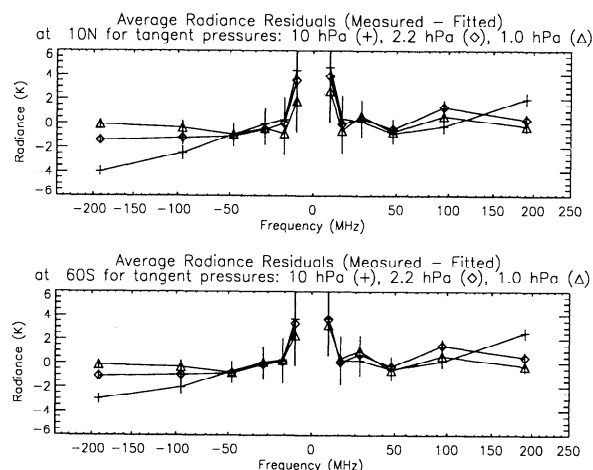
### 4.2. Residuals From Measurements

The next set of figures shows measured radiances and radiance residuals. Figure 9 is analogous to Figure 5 and shows the radiances for the study MMAF. The measured and simulated radiances have the same overall structure, but the radiance residuals (Figures 6 and 10) are approximately 5–6 times larger for the measurements and have a spectral pattern absent in the simulations. Similar patterns are seen in the zonally

averaged residuals (Figure 11) at 10°N and 60°S, implying that the large residuals are systematic. The pattern of the radiance residuals, measured by the difference in residual between adjacent channels or symmetric channels (e.g., channels 15 and 1), is approximately independent of latitude. Figure 12 shows radiance residuals at 10 hPa for individual gridded scans on the 10°N and 60°S latitude circles. Comparisons with corresponding simulation residuals (Figure 8) suggest that measured residuals can be represented as the sum of a globally

Radiances for MMAF: 579488 for tangent pressures:
10 hPa (+), 2.2 hPa (◇), 1.0 hPa (△)

**Figure 9.** Measured radiances from reference scan. Symbols are the same as in Figure 5.

Radiance Residuals (Measured – Fitted)
at 10N, 10 hPa at longitudes: 7E (+), 82E (*), 180E (◇), 269E (△)

Radiance Residuals (Measured – Fitted)
at 60S, 10 hPa at longitudes: 6E (+), 88E (*), 186E (◇), 269E (△)
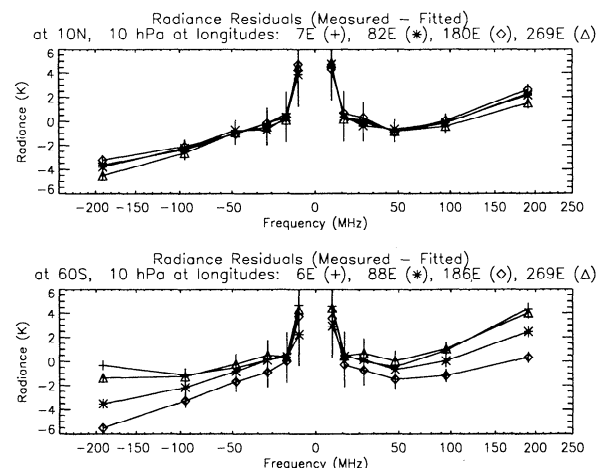
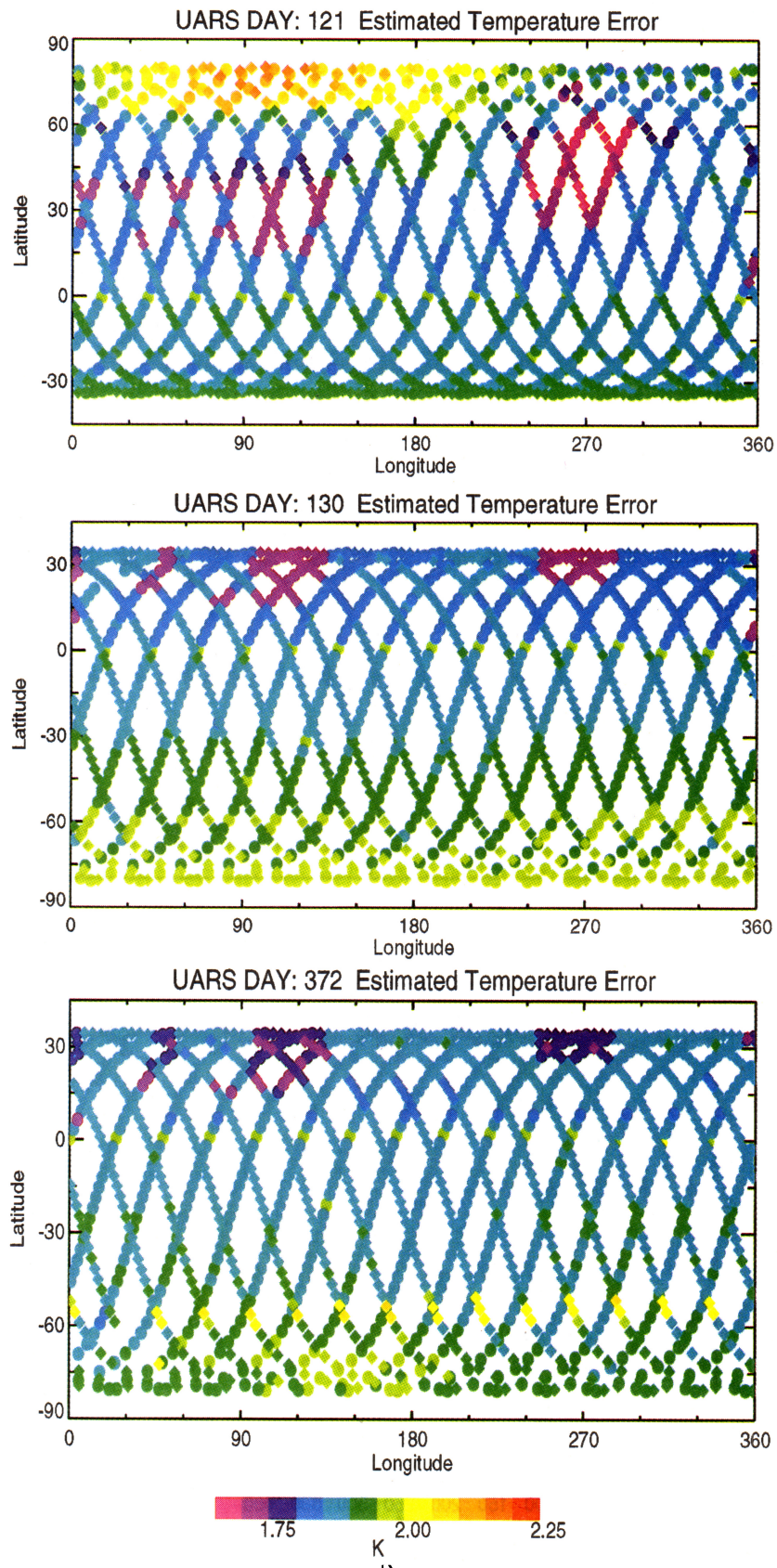**Figure 12.** Same as Figure 8 but for measured radiances.

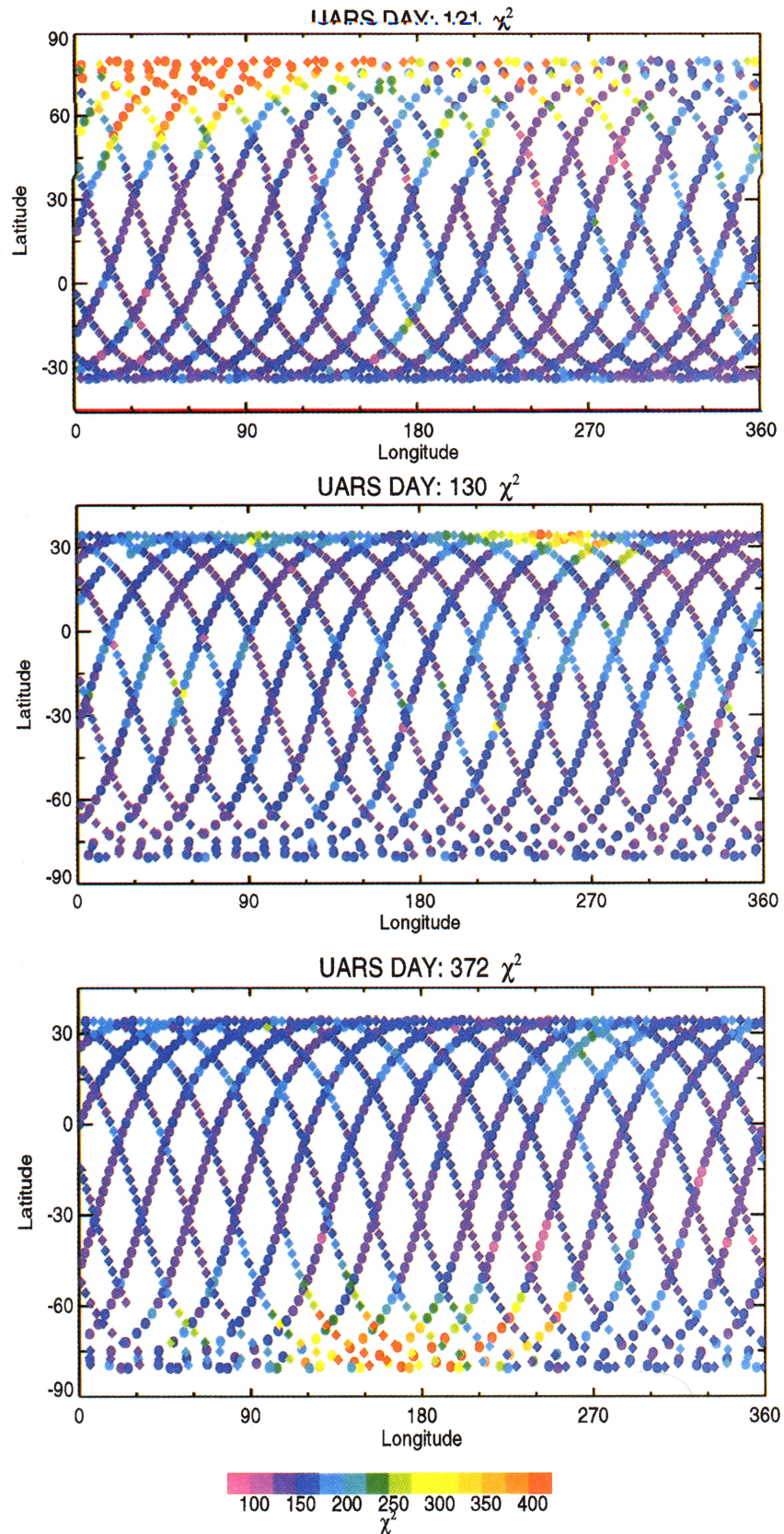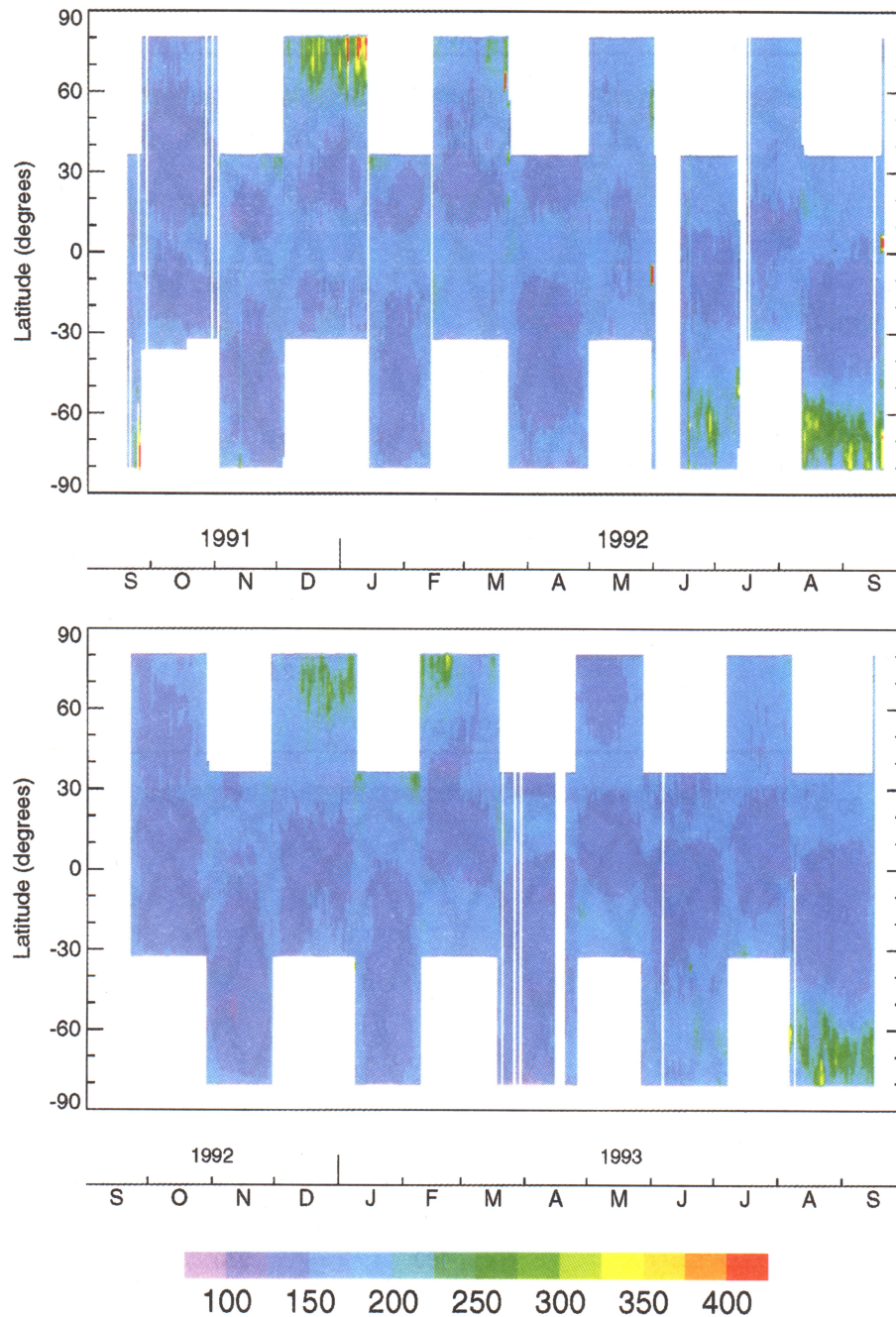**Plate 4.** Estimated uncertainty of 10 hPa temperature for the days shown in Plate 3.

**Plate 5.** Values of $\chi^2$ for the days shown in Plate 3.

**Plate 6.** Time series of zonally averaged $\chi^2$ for the first 2 years of Microwave Limb Sounder (MLS) operations.

averaged residual plus perturbations. The perturbation residuals have many similarities to the simulation residuals; they are approximately symmetric around band center and have approximately the same deviation, although values for corresponding scans are not equivalent. The globally averaged residual is approximately the 10°N zonally averaged residual and has a strong antisymmetric (around band center) spectral signature not present in the simulations. It is probably caused by an error in the measurement model, and the following subsections identify potential errors. Differences in $\chi^2$ between measurements and simulations are associated

with a large globally averaged residual in the measurements, and although both measurement and simulation have comparable residual deviation, the cross term in the squared residual accounts for the greater variations in $\chi^2$ for measurements.

### 4.3. Spectral Signature of Retrieved Parameters

This subsection examines the spectral signatures of retrieved parameters in order to show that the radiance residuals are not easily fit by reasonable values of atmospheric parameters. Figures 13, 14, and 15 show the spectral signatures for perturbations in tangent-
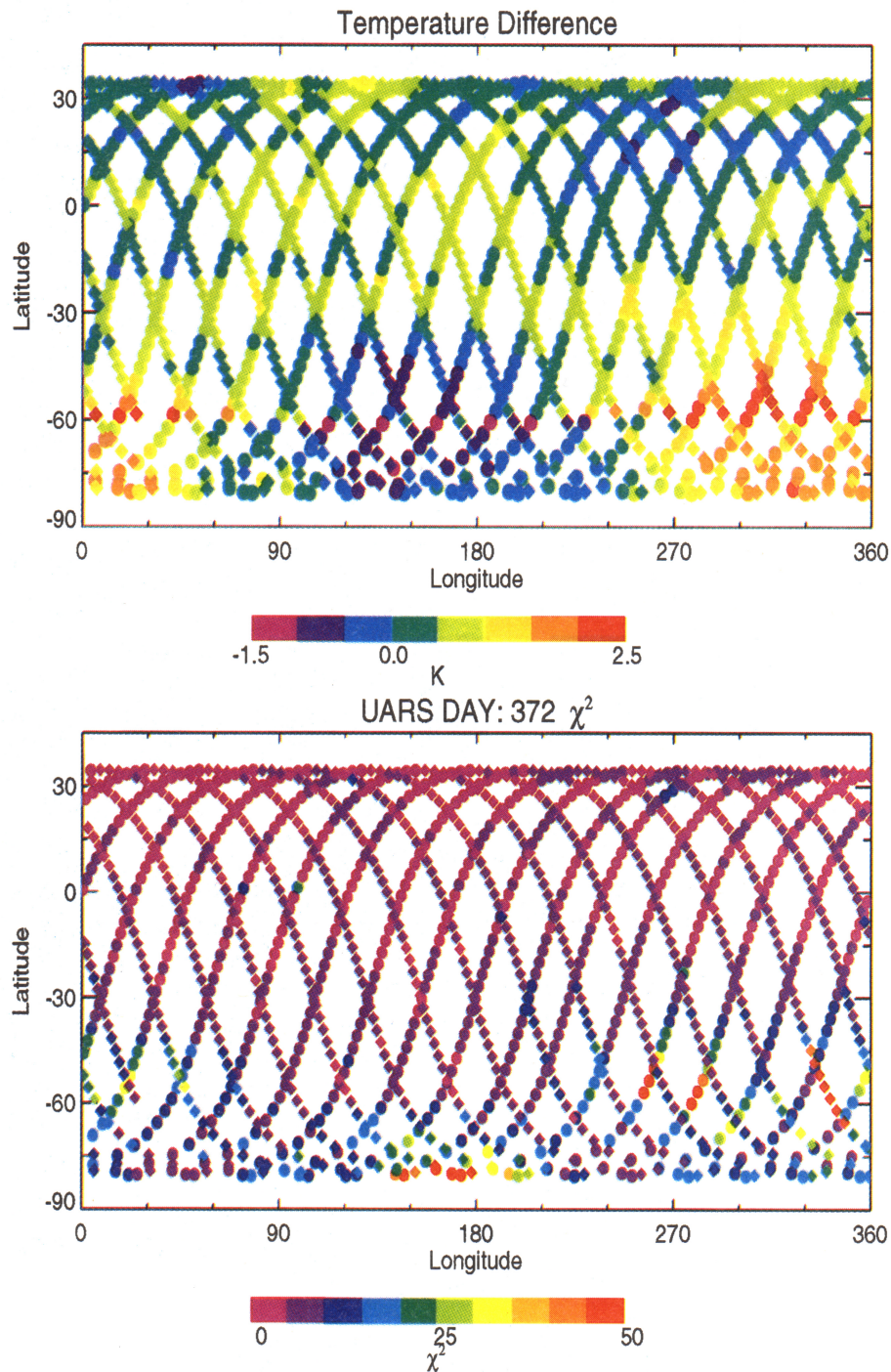
**Plate 7.** Temperature uncertainty (retrieved values – model values) and $\chi^2$ at 10 hPa for a full day of simulated retrieval.

point pressure, temperature, and LOS velocity. The response to a 100-m offset in tangent-point pressure is a symmetric broadening of the emission. Temperature perturbations also produce symmetric spectral features, and while LOS velocity has a weak antisymmetric spectral signature, a velocity greater than 100 km/s (which is unrealistic) is needed to produce a 4 K spectral difference across the filter bank bandpass. In summary, the spectral residuals observed in measurements cannot be represented with perturbations to the atmospheric state.

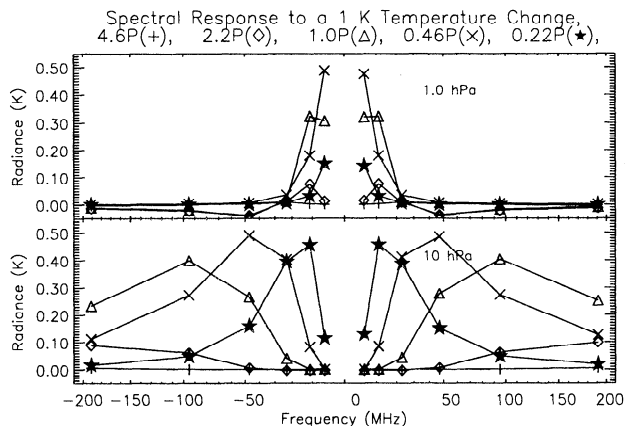### 4.4. Spectral Signature of Errors in the Instrument Model

The possibility that observed radiance residuals are produced by instrument model errors is explored in this section. The three largest sources are errors in radiometric gain, antenna FOV, and sideband ratio. Errors in the accuracy of the radiometric gain (mostly losses in the optical path in front of the switching mirror) produce radiance residuals proportional to the measured radiance and have symmetric spectral signatures since

Spectral Response to a −100m offset at
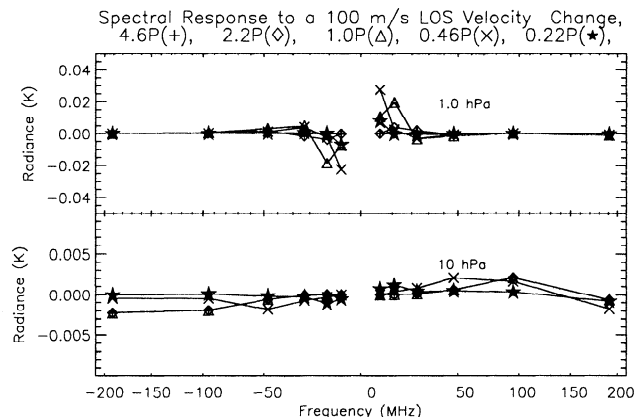10 hPa(◊), 1 hPa(×), and 0.1 hPa(★)
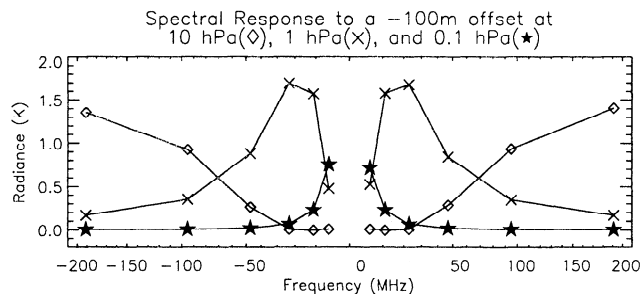


**Figure 13.** Spectral signature of a 0.1 km offset in tangent point pressure for tangent points at 0.1 hPa (stars), 1 hPa (crosses), and 10 hPa (diamonds).

Spectral Response to a 100 m/s LOS Velocity Change,
4.6P(+), 2.2P(◊), 1.0P(△), 0.46P(×), 0.22P(★),



**Figure 15.** Spectral signature at (top) 1 hPa to a 100 m/s line of sight (LOS) velocity increase (towards MLS) at 0.22 hPa (stars), 0.46 hPa (crosses), 1 hPa (triangles), 2.2 hPa (diamonds), and 4.6 hPa (pluses); (bottom) 10 hPa to a 100 m.s LOS velocity increase at 2.2 hPa (stars), 4.6 hPa (crosses), 10 hPa (triangles), 22 hPa (diamonds), and 46 hPa (pluses).

the radiances are symmetric. Figure 16 shows the spectral signature of a 3% decrease in the width of the antenna FOV. Although radiance residuals of the order of 1 K are consistent with the accuracy of the antenna FOV pattern, the spectral slopes are mostly symmetric. In summary, errors in radiometric gain, or antenna FOV, do not produce antisymmetric spectral signatures and cannot cause the observed measurement radiance residuals.

Sideband ratio varies smoothly from channel to channel, and errors in sideband ratio are expected to be strongly correlated between adjacent channels. Figure 17 shows the nominal sideband ratio, the radiance contribution from each sideband, and the spectral signature of a 10% increase in sideband ratio across the filter bank. Errors in sideband ratio produce errors in radiance only when the radiance contributions from the two sidebands are unequal. Figure 17 shows the radiance contributed from each sideband for the study MMAF of the simulation atmosphere. The radiance error is equal to the product of the difference in radiance contributions from each sideband times the error in sideband ratio. The channel dependence of errors in sideband ra-

tio is under investigation, but a 10% error produces an antisymmetric spectral signature of approximately the right size and shape in the outer channels.

On the basis of our analysis of radiance residuals and spectral signatures of model parameters and instrument calibration parameters, we can make several assertions concerning the large $\chi^2$ values. Large $\chi^2$ is associated with antisymmetric spectral residuals, which are most likely produced by errors in the sideband ratio used in Version 3 processing. Antisymmetric spectral residuals cannot be represented as a superposition of perturbations to retrieved parameters (which are symmetric) and therefore contributions to $\chi^2$ arising from antisymmetric spectral residuals are not expected to correlate with errors in retrieved parameters. The symmetric component in the simulated radiance residual is expected to correlate with errors in retrieved parameters, and the presence of a symmetric residual possibly indicates that the state vector is overly constrained. Lastly, $\chi^2$ is dominated by an antisymmetric residual, and it is likely that $\chi^2$ is only a marginally useful diagnostic of retrieved parameter quality, but variations in $\chi^2$ are probably indicative of changes in the quality of geophysical parameters, especially in the midstratosphere.

Spectral Response to a 1 K Temperature Change,
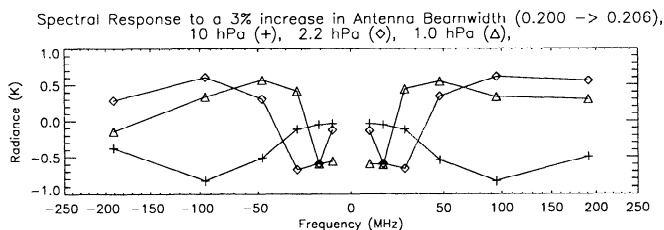4.6P(+), 2.2P(◊), 1.0P(△), 0.46P(×), 0.22P(★),



**Figure 14.** Spectral signature at (top) 1 hPa to a 1 K increase in temperature at 0.22 hPa (stars), 0.46 hPa (crosses), 1 hPa (triangles), 2.2 hPa (diamonds), and 4.6 hPa (pluses); (bottom) 10 hPa to a 1 K increases at 2.2 hPa, 4.6 hPa, 10 hPa, 22 hPa, and 46 hPa.

Spectral Response to a 3% increase in Antenna Beamwidth (0.200 −> 0.206),
10 hPa (+), 2.2 hPa (◊), 1.0 hPa (△),



**Figure 16.** Spectral response to a 3% increase in width of antenna field of view (FOV) at 1 hPa (triangle), 2.2 hPa (diamond), and 10 hPa (pluses).
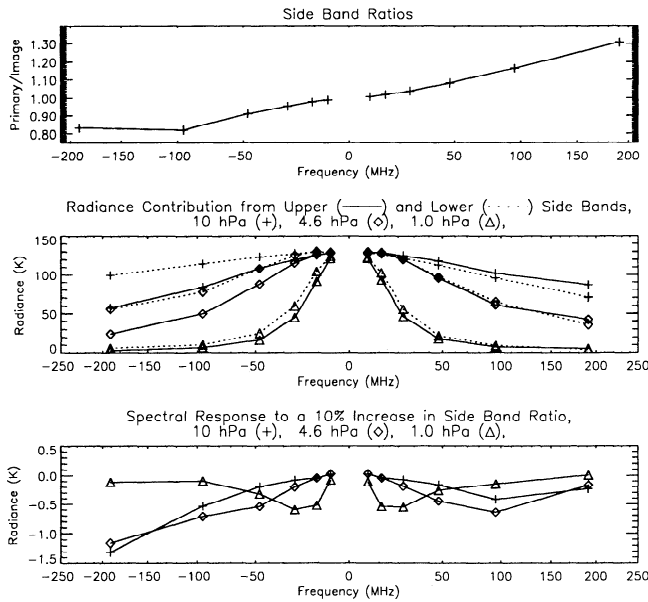
**Figure 17.** Measured sideband ratios, radiance contribution from the upper and lower sidebands, and the spectral signature from a 10% increase in sideband ratio (top to bottom). In the middle panel, contributions from the upper and lower sidebands are represented by solid and dotted lines. Radiance contributions and spectral signatures in the middle and bottom panels are shown at 1 hPa (triangles), 4.6 hPa (diamonds), and 10 hPa (pluses).

## 5. Estimated Error Budget

The retrieved profile can be represented as the sum of the real profile plus error terms. Following the formalism of *Rodgers* [1990], the solution error covariance can be decomposed into (1) a contribution from measurement noise

$$S_M = DE_M D^T , \quad (5)$$

(2) smoothing error arising from failure of the averaging kernels to reproduce the true state,

$$S_S = (A - I)S(A - I)^T , \quad (6)$$

and (3) model parameter errors arising from inaccuracies in instrument characterization, spectroscopic parameters and constrained parameters, and approximations in radiance calculations

$$S_B = D \left( K_b S_b K_b^T + E_f \right) D^T , \quad (7)$$

where $K_b$ is the matrix of model parameter weighting functions $(K_b = \partial y^c / \partial b)$ and $S_b$ is the covariance matrix for model parameters. The constrained parameter covariance matrix $S_c$, mentioned in section 3, is a block within $S_b$. The extraneous radiance error-covariance, also listed in section 3, is a block of $K_b S_b K_b^T$. The forward model error-covariance, $E_f$, has been separated from $K_b S_b K_b^T$ because of the difficulty of defining parameters which characterize this error source.

The decomposition of the error budget into precision and accuracy depends on the timescale of the variability of the error source. Sources such as measurement error vary on the shortest timescales (2 s between MMIFs) and contribute only to the precision, while others such as smoothing error are systematic and contribute only to the accuracy. Model parameter errors may be systematic or may vary on any timescale [*Rodgers*, 1990], and a proper decomposition requires examining the measurement system model and the properties of each parameter. To facilitate this analysis, model parameter errors have been subdivided into categories consisting of instrument characterization errors, spectroscopic and geophysical parameter errors, and forward model errors.

Model parameter errors varying on intermediate timescales can produce biases that can be mistaken for atmospheric variability. For example, if the model parameter $b(t)$ has an assumed value $b^*$, the estimated state is biased by $DK_b(b^* - b(t))$. The time average of the variance in $b$ propagated through equation (7) provides an estimate of the model parameter error, but since all information concerning time variability is lost, the estimated error should be assumed to vary on all timescales. If the power spectra $P_b$ of the variance of $b$ can be estimated, at least for the dominant frequencies, then the time variance in model parameter errors can also be estimated [see *Papoulis*, 1965, pp. 344–352]. Specifically, we are interested in periodic errors, where $P_b(T)$ is the total power spectrum of the variance of $b$ in all harmonics of period $T$. The amplitude of the error with period $T$ is $S_b(T) = DK_b P_b(T) K_b^T D^T$. The confidence that a periodic signal in a retrieved parameter is not erroneous is determined by the ratio of the amplitude of the signal divided by the power in the error covariance $S_b(T)$. Many instrument parameters (e.g., extraneous
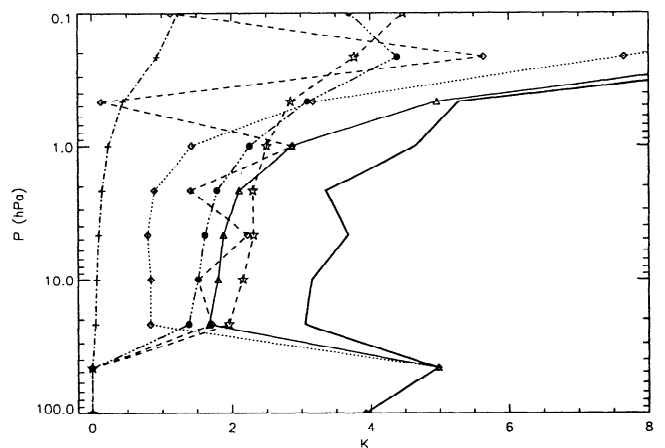


**Figure 18.** Sources for temperature errors. The thick solid line is the total accuracy and is the rss of precision (dashed-dotted line), smoothing error (dotted line with diamonds), instrumental accuracy (dashed line with stars), forward model noise accuracy (dashed line with diamonds), and forward model errors (dashed-triple dotted line with circles). The uncertainty contained in the Level 2 and Level 3 files is shown by a solid line with triangles.
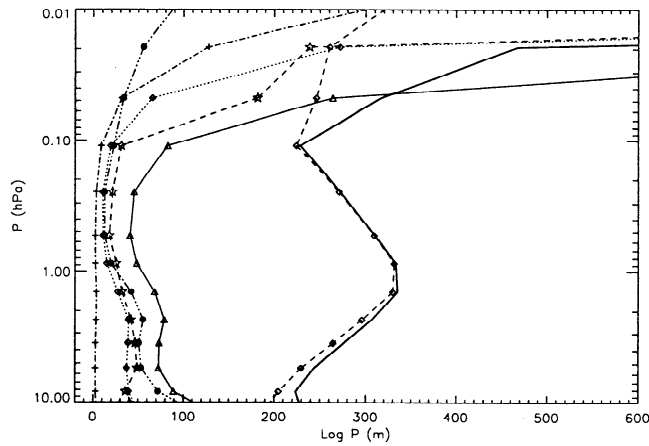
**Figure 19.** Error sources for tangent-point pressure. The symbols and line styles are for the same contributions as in Figure 18.

radiance and radiometric gain) have errors with large fractions of their power at the period of the UARS yaw period. Sun-synchronized waves can also be aliased to the same period, so by estimating the amplitude of fluctuations in retrieved parameters from instrument model parameters, we will estimate the smallest atmospheric wave synchronized to the UARS yaw period that can be resolved.

### 5.1. Measurement Noise Errors

Measurement noise error, shown in Figures 18 and 19 contribute to the precision budget and are generally less than 0.5 K for temperature and less than 20 m for tangent-point pressure. Measurement error increases in the mesosphere where most of the retrieval sensitivity comes from the inner channels which have greater noise. Time series of radiance noise show little variability, and all studies indicate that radiance noise is stationary during normal MLS operations.

### 5.2. Smoothing Errors

Smoothing error is also shown in Figures 18 and 19, and is generally less than 1 K for temperature from 22 hPa to 1 hPa and less than 40 m for tangent-point pressures from 10 to 0.1 hPa. Smoothing errors dominate the error budget when the information content of the measurements becomes comparable to the a priori uncertainties. In the case of the Version 3 product, temperature errors above 0.46 hPa relax to the a priori error because channels 1–6 and 10–15 are not sensitive to temperature at these levels; while below 22 hPa (10 hPa for tangent-point pressure), the smoothing error is artificially high because temperature and tangent-point pressure are not retrieved.

### 5.3. Instrument Parameter Errors

Errors in instrument parameters contributing to the precision, accuracy, and stability error budgets are listed in Table 1. The cumulative errors from all instrument parameters are shown in Figures 18 and 19. Errors in

instrument parameters generate some of the largest inaccuracy for retrieved temperature; temperature accuracy is typically greater than 1.5 K and can be as large as 2.8 K at 0.46 hPa. For tangent-point pressure, instrumental effects are a small component of the inaccuracy, generating less than 50 m from 10 hPa to 0.1 hPa.

The contributions to temperature errors from individual instrument parameters are shown in Figure 20. Radiometric gain is the largest source, with FOV and extraneous radiance providing smaller amounts; the sideband ratio contribution is a factor of 2 smaller. Errors in sideband ratio are the likely cause of poor radiance closure but have a small contribution to the temperature errors, because they produce an antisymmetric spectral signature that is orthogonal to the spectral signature of the retrieved parameters (compare Figures 14 and 17).

Extraneous radiance varies both over an orbit and a yaw period but has the largest power synchronized to the yaw period. The rms variation is estimated to be a third of the average power, and the resulting errors are shown in Figure 20. Yaw-period synchronized variations in temperature below 0.46 hPa are less than 0.2 K from this error. Orbit-synchronized variations (not shown) are less than 0.05 K. Radiometric calibration also varies over an orbit and yaw period, but its influence is less than 0.02 K.

### 5.4. Spectroscopic and Constrained Parameters

Constrained parameters in the Version 3 processing are listed in Table 1 and include LOS velocity, $O_2$ and $^{18}OO$ mixing ratios, and temperature below 22 hPa. Constrained parameters primarily affect the precision, provided the value of the constrained parameter is not biased. LOS velocity produces errors less than 0.02 K
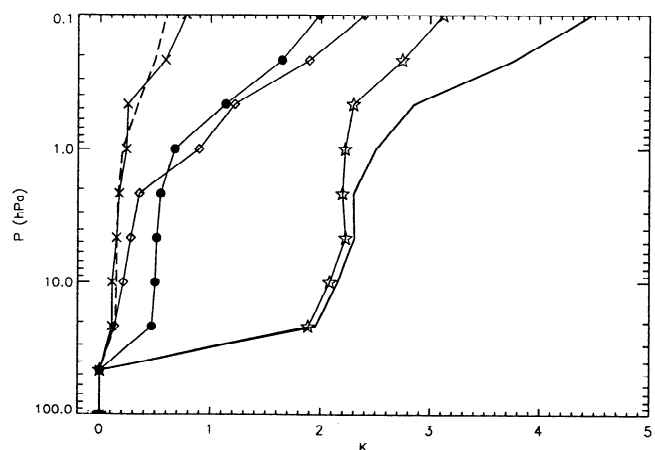


**Figure 20.** Contribution to temperature accuracy from instrument parameter errors. The instrument parameter error (thick solid line) is the rss of the radiometric gain error (stars), antenna FOV error (diamond), sideband ratio error (crosses), and extraneous radiance error (circles). Measurement stability over a yaw period from variation in extraneous radiance (dashed line) is also shown.

**Table 3.** Estimated Precision, Accuracy, Bias ($O_2$ Line Width Error), Stability, and Version 3 Uncertainty Estimates for MLS Temperature

| Pressure hPa | Precision K | Accuracy K | Bias K | Stability K | Version 3 K |
|---|---|---|---|---|---|
| 0.46 | 3.1 | 5.1 | -0.1 | 0.34 | 6.4 |
| 1.0 | 2.3 | 4.6 | -2.9 | 0.20 | 3.4 |
| 2.2 | 1.8 | 3.3 | -1.4 | 0.16 | 2.2 |
| 4.6 | 1.6 | 3.7 | -2.2 | 0.15 | 2.1 |
| 10 | 1.5 | 3.1 | -1.5 | 0.15 | 1.9 |
| 22 | 1.4 | 3.0 | -1.7 | 0.14 | 1.8 |

in temperature and 4 m in tangent-point pressure; $O_2$ mixing ratio generates errors less than 0.02 K and 2 m; and the other sources contribute comparable errors. In summary, constrained parameters are not a significant error source.

Spectroscopic parameters include line strengths, frequencies, and pressure broadening coefficients and contribute to the accuracy and bias error budgets. The contributions from line strength and frequency uncertainties to temperature errors are less than 0.1 K at all levels. Inaccuracy in the line-broadening parameter dominates the error from these sources. It is believed to be biased 6% high, and temperature and tangent-point pressures changes for a 6% decrease in line-broadening parameter are presented in Tables 3 and 4; these should be subtracted from the temperatures appearing in MLS Version 3 files, or the tangent-point pressures in the Level 2 files.

### 5.5. Forward Model Noise

Forward model noise is associated with numerical approximations in the forward model and is in principle related to model parameters characterizing forward model linearization and numerical truncation that have a covariance matrix $S_f$ and weighting functions $K_f$. The forward model error covariance $E_f = K_f S_f K_f^T$ is expected to have nonzero off-diagonal elements. However, the retrieval algorithms assume $E_f$ is diagonal, and because this ignores possible correlations between elements, the resulting uncertainties are probably overestimated. Figures 18 and 19 show that these errors are some of the largest contributors to the error budgets for temperature, contributing 1–2 K for temperatures from 22 hPa to 1 hPa. For tangent-point pressure, forward model noise is a less important error source, generally contributing less than 75 m. Forward model noise depends on the degree to which the atmospheric state varies from the linearization state and affects both the accuracy and the precision. The fraction attributed to accuracy and precision has not been estimated, and forward model noise is here wholly budgeted to both. Generally, greater atmospheric variability leads to larger forward model noise errors, and forward model noise is expected to be larger during winter, especially in the north. The forward model error covariance $E_f$ is an 'average' estimate over a range of conditions and may

underestimate errors in the forward model in winter at high latitudes and overestimate them near the equator.

### 5.6. Summary of Estimated Errors

The results of this section are summarized in Tables 3 and 4 for temperature and tangent-point pressure, respectively. The uncertainties contained in Version 3 files are also shown for comparison and tend to be closer to the estimates of precision than accuracy.

## 6. Comparisons with other data sets

Accuracy estimates are obtained through comparison of MLS temperatures with other data sets in this section.

### 6.1 NMC Comparisons

The NMC daily analyses provide a continuous global record of stratospheric temperature spanning several decades [*Gelman et al.*, 1986] and has been incorporated in a large number of intercomparison studies [e.g., *Ferrare et al.*, 1995; *Finger et al.*, 1993; *Gelman et al.*, 1986; *Keckhut et al.*, 1994; *Remsberg et al.*, 1992, 1994; *Wild et al.*, 1995]. In this subsection the NMC daily analyses are sampled at the MLS retrieval locations, and comparisons are made in zonal means and in mapped differences. The NMC analysis incorporates global Tiros Operational Vertical Sounder (TOVS) soundings and northern hemisphere radiosondes below 5 hPa in separate hemispheric analyses based on a modified Cressman algorithm [*Finger et al.*, 1965]. Daily 1200 UT temperature maps are produced at 30, 10, 5, 2, 1, and 0.4 hPa [*Gelman and Nagatani*, 1977]. For the 1991–1993 period, TOVS sounding are provided by the NOAA 11 satellite, which is in a Sun-synchronized polar orbit with equator crossings at 1530 and 0330 LT. The NMC analyses use data from 0600 UT through 1800 UT, so that TOVS data at any location is either from the early morning or from the afternoon sounding. Estimated errors are provided by NMC and are between 2 K and 3.5 K at 30 hPa and 10 hPa, depending on location and height, and are 5, 6, 7, and 9 K at 5, 2, 1, and 0.4 hPa. NMC temperatures have been

**Table 4.** Estimated Precision, Accuracy, Bias ($O_2$ Line Width Error), Stability, and Version 3 Uncertainty Estimates for MLS Tangent-Point Pressure

| Pressure hPa | Precision m | Accuracy m | Bias m | Stability m | Version 3 m |
|---|---|---|---|---|---|
| 0.046 | 50 | 320 | 250 | 270 | 30 |
| 0.10 | 25 | 230 | 220 | 8 | 90 |
| 0.22 | 15 | 260 | 260 | 2 | 50 |
| 0.46 | 10 | 310 | 300 | 1 | 40 |
| 1 | 25 | 340 | 340 | 3 | 50 |
| 2.2 | 55 | 310 | 300 | 5 | 80 |
| 4.6 | 50 | 260 | 240 | 6 | 75 |
| 10 | 90 | 220 | 200 | 5 | 110 |
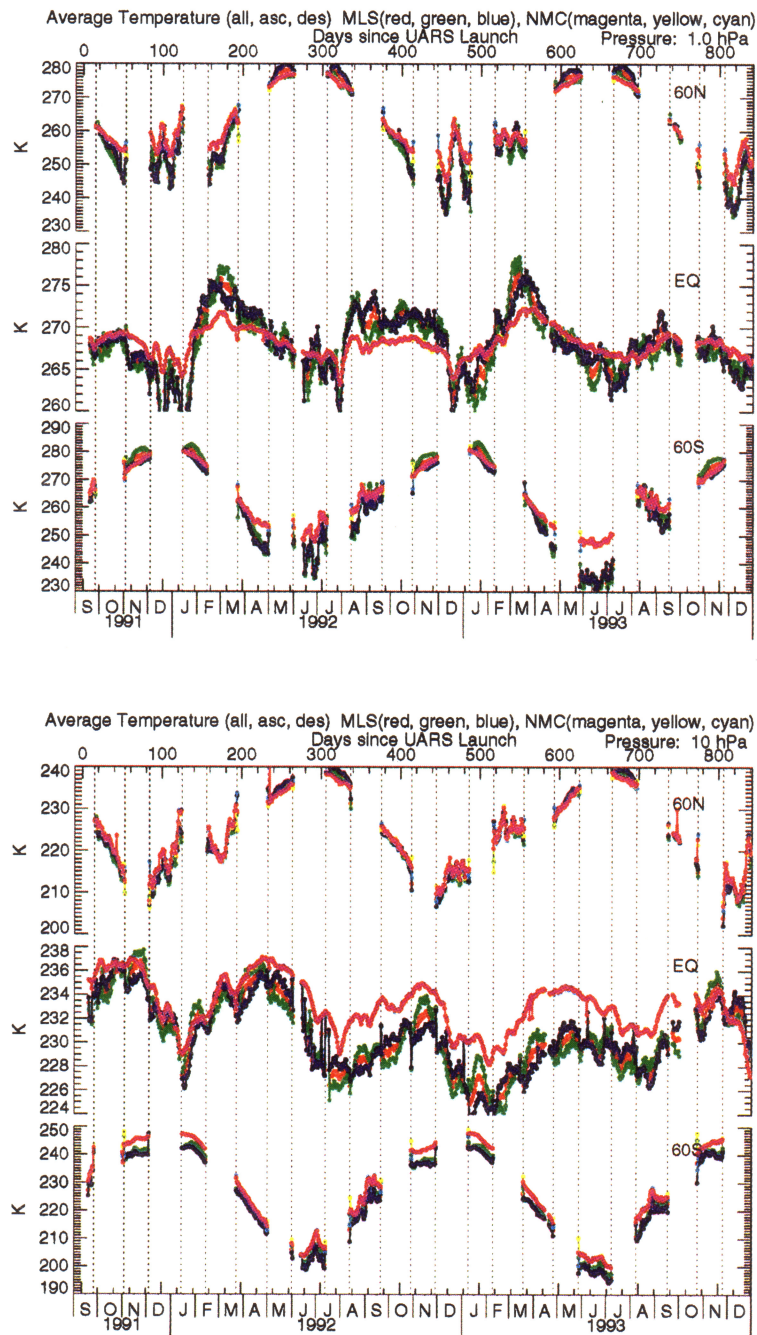
**Plate 8.** Time series of MLS and National Meteorological Center (NMC) zonally averaged temperatures at 10 hPa and 1 hPa for 10° latitude bins centered on 60° S, 0°, and 60° N. The NMC and MLS are binned by ascending data (yellow for NMC, green for MLS), descending data (cyan, blue), and combined data (magenta, red). For the NMC data, ascending, descending, and combined data time series are pratically identical, and only the combined curve is visible.

corrected for average bias errors determined from comparison with rocketsonde profiles [*Gelman et al.*, 1994].

The data sets are compared profile by profile. The NMC analyses are linearly interpolated to the MLS profile locations without correcting for diurnal variations. Differences between the data sets are indicative of potential errors in each data set, diurnal variability, or differences in resolution. With regard to resolution the most significant differences include the 15 to 20-km-

wide TOVS vertical weighting functions [*Smith et al.*, 1979] versus the 5.4-km MLS retrieval grid and horizontal smoothing in the NMC analyses versus horizontal smearing over an MLS scan.

Zonal averages of MLS and NMC temperature at 1 and 10 hPa for 60°N, 60°S and equatorial, 10° wide latitude bins are shown in Plate 8. At 10 hPa, MLS is generally 2 K colder than NMC except during northern summer. At the equator, MLS and NMC temper-
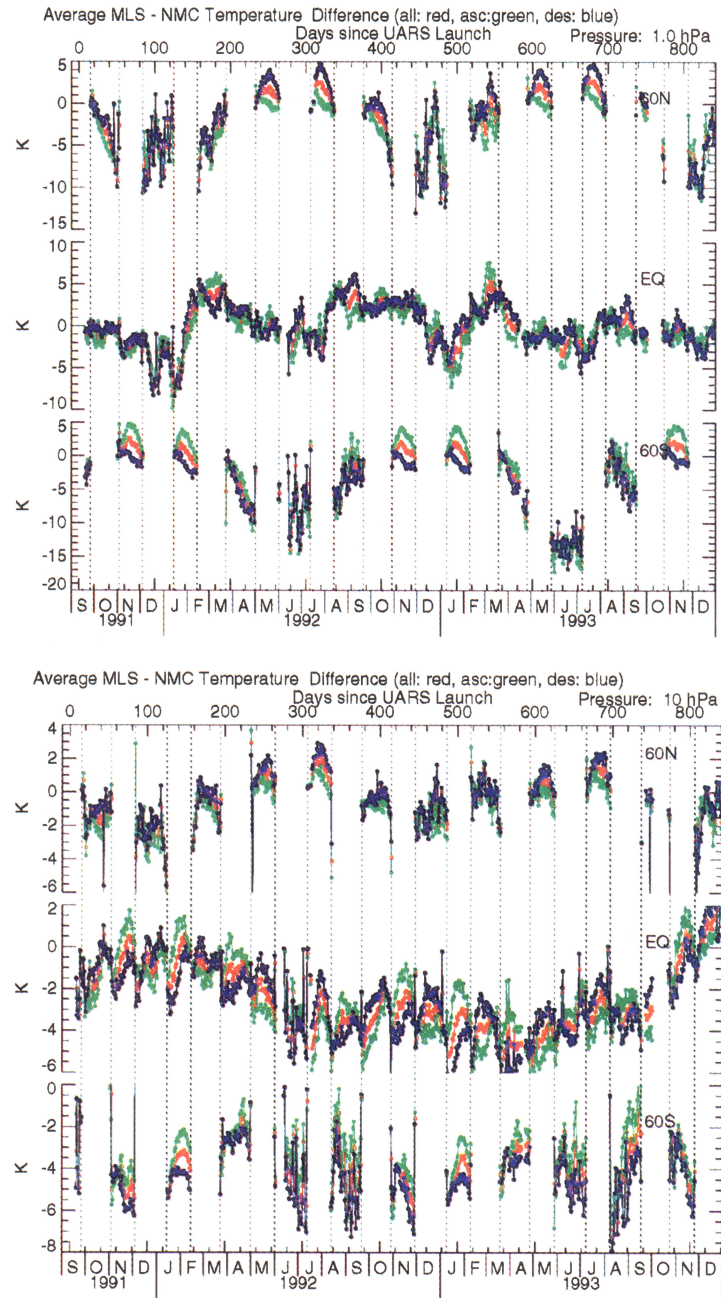
**Plate 9.** Time series of MLS - NMC zonally averaged temperature differences for the same levels and latitude bins as in Plate 8. Differences for ascending, descending, and all data are green, blue, and red, respectively.

atures agree to within 2 K during the first 200 days of operation, but MLS becomes approximately 5 K colder starting in April 1992 and remains so until November 1993. The agreement at 1 hPa is noticeably worse, especially on some winter days at high latitudes where MLS temperatures are approximately 15 K lower than NMC. Transients associated with wave forcing such as the stratospheric sudden warmings, the equatorial sudden cooling, and the semiannual oscillation (SAO) are consistently stronger in the MLS field at all levels.

Zonal mean differences are shown in Plate 9. The differences have a strong annual oscillation, which at 10 hPa is approximately 4 K peak-to-peak at high latitudes and 2 K near the equator. The 10 hPa cooling at the equator starting in April 1992 appears to be correlated to the quasi-biannual oscillation (QBO); MLS temperatures show a larger-amplitude QBO. At 1 hPa the annual oscillation in MLS temperatures is approximately 15 K peak to peak at 60°S, 10 K at 60°N and less than 2 K at the equator. The SAO dominates the annual cycle at the equator at 1 hPa and is approximately 10 K peak to peak larger in MLS. Equatorial differences at 1 hPa during November and December 1991 and 1992 oscillate with a 4 K amplitude, and a com-

parison of the temperature time series (Plate 8) shows oscillations that are approximately 2–3 times larger in MLS temperatures. The SAO and QBO are associated with planetary wave activity [*Andrews et al.*, 1987], and differences between MLS and NMC temperatures indicate that the signatures of dynamics associated with planetary waves tend to be larger in the MLS temperatures.

The zonal mean difference shows a 72-day oscillation, a discontinuous change in temperature across yaw maneuvers, and differences between averages from data on the ascending and descending sides of the orbit (shown in Plates 8 and 9). Part of the explanation for these features arises from the precession of the UARS orbit through 12 hours of solar time every 36 days and the discontinuous change in solar time during a yaw maneuver. Sun-synchronized waves are aliased onto oscillations of the zonal mean with periods equal to 72 days divided by the zonal wavenumber (e.g., the diurnal and semidiurnal component are aliased to 72- and 36-day oscillations), and the differences between sides of the orbit or across yaw maneuvers could be associated with the MLS sampling of weakly modulated, Sun-synchronized waves. However, systematic errors associated with extraneous radiances could produce similar effects. There are several reasons for believing most of these differences are not instrumental. First, the differences between zonal averages on each side of the orbit are often as large as the variation over the yaw period, while extraneous radiances vary much less over an orbit than over a yaw cycle. Secondly, the yaw period oscillation of insolation is modulated by the yearly cycle and a similar modulation is not seen in the temperature oscillation. Lastly, discontinuous changes in solar time at equatorial tangent points across yaw maneuvers seem to be correlated to solar time dependence of Sun-synchronous waves. For example, at the equator, solar time regresses 3.6 hours earlier on one side of the orbit, placing it at the same solar time as 11 days earlier on the same side of the orbit. The temperature discontinuity between days at the same solar time but 11 days apart tends to be much smaller than between days immediately across the yaw maneuver but at different solar times. The ascending side of the orbit around 29 October 1992 and the descending side of the orbit on 21 September 1992 at 10 hPa seem to illustrate this correlation, but there are several instances where the correlation is weak, or the time shift seems to be greater than 11 days. Finally, if the differences between temperatures on ascending and descending sides of the orbit are due to Sun-synchronized waves, then waves other than the diurnal tides must be present.

Figure 21 shows profiles of zonal average MLS and NMC temperatures at the equator, middle and high latitudes on 10 January, 19 January, and 17 September 1992, and addresses differences arising from vertical resolution. MLS profiles show more variability in the structure of the stratopause and often (e.g., equatorial 10, 19 January and southern winter high latitudes, 17 September) do not show the stratopause below
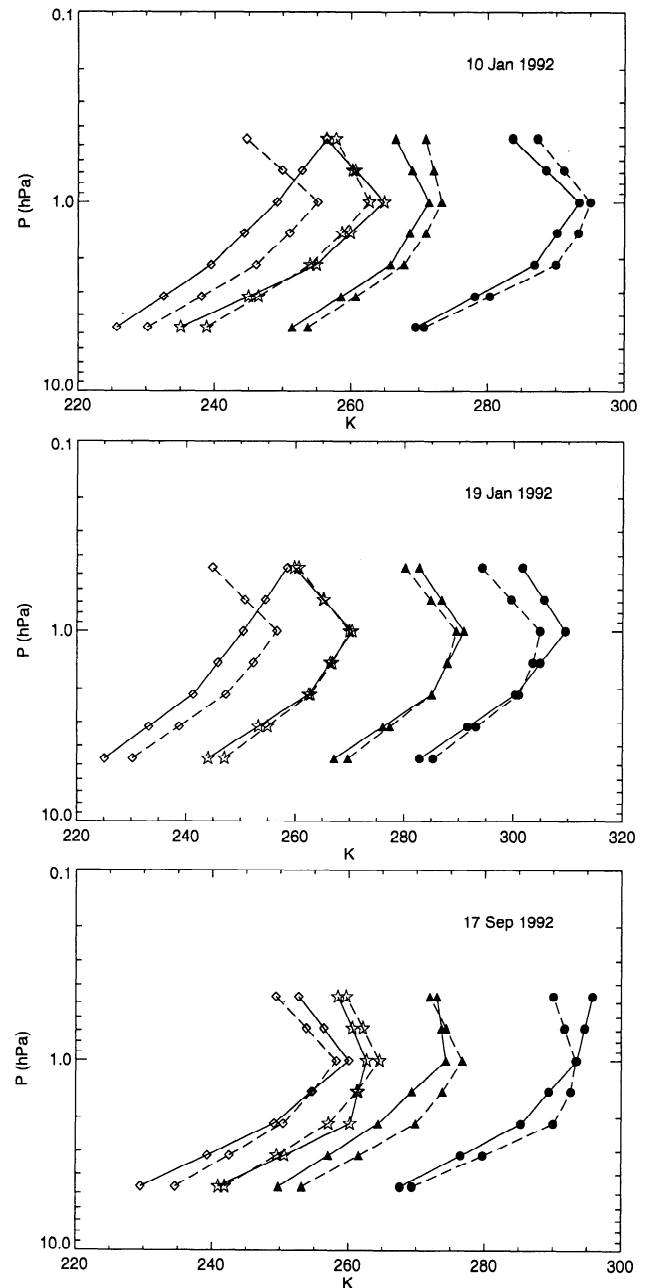


**Figure 21.** Profiles of zonal mean MLS and NMC temperatures for 10 January, 19 January, and 17 September 1992. The MLS profile is shown as a solid line while the NMC profile is shown as a dashed line. Averages are for latitude bins from 5° S – 5° N (diamonds), 25° – 35° (stars), 55° – 65° (triangles), and 75° – 80° (circles); and the profiles are shifted -10 K, 0 K, 10 K, and 20 K. The nonequatorial bins are north latitudes for 10 January and south latitudes for 19 January and 17 September.

0.46 hPa, or show a more pronounced stratopause (e.g., northern winter high latitudes). The NMC corrections are derived from rocketsonde comparisons primarily in midlatitudes and since they are average conditions do not reflect observed differences at high and low latitudes, especially high latitude winter and summer [*Finger et al.*, 1993; *Remsberg et al.*, 1992]. The large dif-
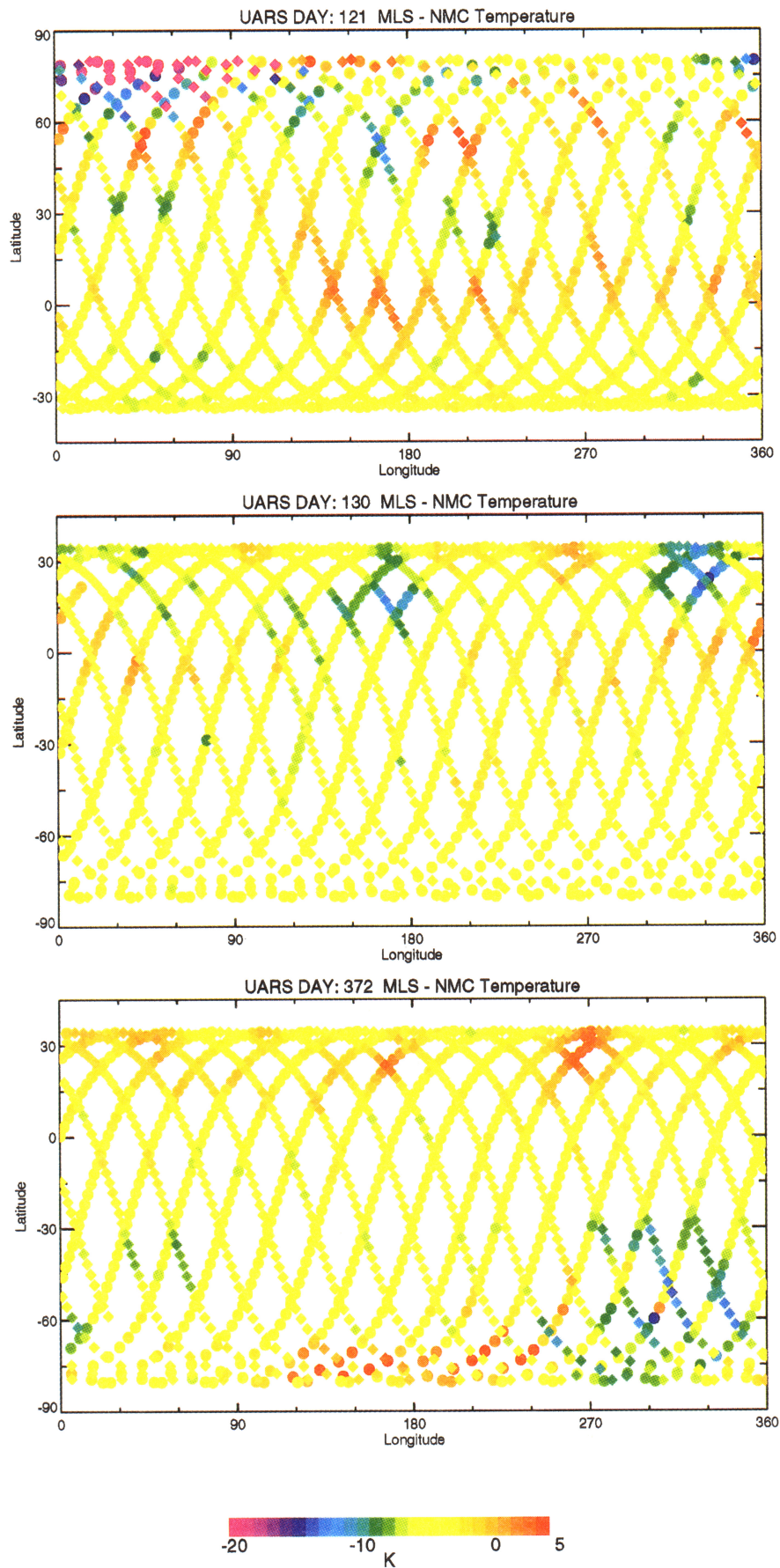
**Plate 10.** Mapped temperature differences at 10 hPa (MLS − NMC) on 10 January 1992, 19 January 1992 and 17 September 1992.

ferences between MLS and NMC temperatures at 1 hPa probably arise from differences in vertical resolution.

Mapped daily MLS – NMC temperature differences at 10 hPa are shown in Plate 10. The largest differences are negative (MLS colder than NMC) and occur in winter at high latitude, usually where horizontal temperature gradients are largest (see Plate 3). At tangent track crossings, disagreement between colocated profiles of more then a few Kelvin indicate either that the atmosphere has changed between measurements (NMC is the same for both profiles) or that an error source in the MLS retrieval is different for the two profiles. Disagreement between colocated profiles is strongest in the winter hemisphere at high latitudes and absent in the summer hemisphere. Traveling planetary waves are strongest in winter at high latitudes, weak in the summer, and are a likely cause. The LOS direction for colocated profiles are usually not collinear and LOS gradients are a potential source of disagreement between colocated profiles. LOS gradients are expected to produce the largest disagreement when the LOS directions for colocated profiles are orthogonal (near 60° in the hemisphere having maximum coverage and 20° in the other) and the least at the extremes of the tangent track. On 10 January near the 65°N, 45°E and on 17 September near 65°S, 225°E, disagreement is greater than 10 K and may be associated with orthogonal LOS directions.

The spatial variability in $\chi^2$ (Plate 5) has features similar to the temperature differences, such as on 10 January near 70°N, 45°E and on 17 September near 75°N, 180°E, which probably arises because the a priori state is primarily the NMC analysis. As discussed in section 3, $\chi^2$ and MLS–NMC squared temperature differences are weakly correlated and the mapped differences show some of the correlation, especially at high latitude on 10 January 1992. Given that LOS gradients are largest here, the large differences between MLS and NMC could indicate a degraded MLS product. At the same time, biasing by the a priori is largest when MLS and NMC temperature differences are large, so some or all of the increased $\chi^2$ may indicate that the 'true' state of the atmosphere is further from the NMC state than indicated by MLS. Finally, at several locations, such as near 30°N, 270°E on 17 September, MLS and NMC temperatures agree even though $\chi^2$ values are large.

Table 5 presents the mean biases between MLS and NMC for each season, at all retrieved levels for low-,

**Table 5.** Zonal Mean Temperature Differences, MLS – NMC for Northern Winter, Northern Spring, Northern Summer and Northern Autumn, Top to Bottom

| P (hPa) | 80° S–55° S | 55° S–25° S | 25° S–25° N | 25° N–55° N | 55° N–80° N |
|---|---|---|---|---|---|
| | | *21 December – 20 March* | | | |
| 0.46 | 5. 1 | -0. 5 | 6. 5 | -4. 2 | 2. 7 |
| 1.0 | 1. 7 | 0. 1 | -0. 5 | -0. 4 | -3. 0 |
| 2.2 | -1. 1 | 1. 0 | -2. 3 | 0. 8 | -4. 6 |
| 4.6 | -2. 3 | -1. 7 | -3. 2 | -1. 2 | -2. 1 |
| 10 | -4. 1 | -3. 3 | -2. 5 | -1. 9 | -1. 1 |
| 22 | -2. 5 | -2. 5 | -1. 2 | -2. 1 | -2. 3 |
| | | *21 March – 20 June* | | | |
| 0.46 | 4. 3 | -0. 6 | 3. 4 | 1. 1 | 7. 0 |
| 1.0 | -7. 8 | -1. 9 | -0. 2 | 0. 2 | 1. 7 |
| 2.2 | -7. 5 | -2. 8 | -0. 7 | 0. 1 | -1. 3 |
| 4.6 | -3. 3 | -1. 9 | -2. 4 | -1. 7 | -2. 1 |
| 10 | -3. 3 | -2. 7 | -2. 7 | -1. 9 | 0. 1 |
| 22 | -2. 7 | -1. 1 | -1. 5 | -2. 4 | -1. 7 |
| | | *21 June – 20 September* | | | |
| 0.46 | 4. 6 | -2. 9 | 3. 2 | 0. 0 | 5. 8 |
| 1.0 | -3. 8 | -1. 7 | -0. 3 | -0. 1 | 2. 4 |
| 2.2 | -4. 8 | -1. 4 | -1. 2 | 0. 5 | -0. 9 |
| 4.6 | -4. 1 | -1. 8 | -2. 9 | -1. 5 | -1. 0 |
| 10 | -4. 5 | -3. 7 | -2. 6 | -0. 9 | 1. 0 |
| 22 | -6. 5 | -2. 6 | -1. 9 | -1. 1 | 0. 2 |
| | | *21 September – 20 December* | | | |
| 0.46 | 6. 3 | 0. 9 | 2. 5 | 0. 7 | 5. 2 |
| 1.0 | 2. 8 | -0. 1 | -0. 5 | -1. 1 | -5. 8 |
| 2.2 | -1. 8 | -0. 0 | -0. 7 | -1. 9 | -6. 1 |
| 4.6 | -3. 9 | -2. 5 | -2. 2 | -2. 2 | -2. 8 |
| 10 | -3. 2 | -4. 7 | -2. 6 | -1. 7 | -1. 7 |
| 22 | -0. 2 | -3. 8 | -2. 3 | -1. 0 | -2. 3 |

These averages are constructed from the first 842 days of operation.

middle-, and high-latitude bins. On average, MLS temperatures tend to be 1–2 K colder than NMC temperatures throughout the middle and upper stratosphere, although MLS temperatures are considerably colder (4–8 K) in the fall and winter high latitudes. Differences in stratopause temperature have the most variability and probably reflect the poorer vertical resolution in the TOVS weighting functions. Lastly, time series of differences show variability synchronized to the yaw periods, seasons, and yearly cycle.

## 6.2. Comparisons With Lidar

In this subsection, MLS and lidar temperature profiles are compared. Lidar temperature profiles have sub-kilometer vertical and horizontal resolution and are accurate to around a Kelvin in the upper stratosphere and lower mesosphere. Lidar operate at night, cloud cover permitting, and generally integrate for an hour or more to get 1 K temperature precision. Temperatures are sensitive to small-scale wave disturbances, depending on integration time, and in all cases are sensitive to diurnal variations. Lidars do not provide global coverage and are primarily located in northern midlatitudes. The data sets used here include measurements from the Table Mountain Facility (TMF) California, Observatory of Haute-Provence (OHP) France and the Goddard Spaceflight Center (GSFC) Maryland, and include the Centre National de la Recherche Scientifique (CNRS) 532-nm lidar at OHP [*Chanin and Hauchecorne*, 1981], the Jet Propulsion Laboratory (JPL) 353 nm lidar at TMF [*McDermid et al.*, 1990], and the mobile Statospheric Ozone Lidar Trailer Experiment (STROZ-LITE) 351-nm lidar [*McGee et al.*, 1995] operated at each of the three sites. All instruments retrieve density from the intensity of backscattered Rayleigh luminance and estimate temperature using hydrostatic balance. To minimize the error in estimating differential density from backscattered Rayleigh luminance from aerosols, the STROZ-LITE lidar also uses an $N_2$ backscattered Raman signal which is only weakly affected by aerosols. The locations, approximate integration times, and number of profiles for each data set used in the comparison are summarized in Table 6. The data include the Network for the Detection of Stratospheric Change (NDSC) lidar intercomparisons at OHP and TMF during July-August and February and March 1992 [*Keckhut et al.*, 1994; *Ferrare*

*et al.*, 1995]. The CNRS lidars were adversely affected by the Pinatubo aerosols during the intercomparison period, and temperatures below 34–37 km (4 hPa) are generally cooler than those from STROZ-LITE by 1–2 K.

Lidar profiles are retrieved on altitude grids and are transformed to pressure grids using hydrostatic balance and the NMC pressure at the bottom. When taking differences between MLS and lidar profiles, the lidar profiles are smoothed to the MLS retrieval grid using least squares fitting to the MLS vertical basis functions. MLS profiles are selected for comparison from a 12-hour, 20° latitude by 50° longitude window centered on the lidar measurement. One MLS profile is compared to the lidar profile, using an optimization criterion that minimizes the sum of the geodetic and meridional distances between the lidar station and the MLS tangent point (this criterion takes into consideration that temperature depends more on latitude than on longitude). Profile comparisons are shown for the nearest coincidences, but average differences are computed from all coincidences satisfying the criterion.

During December and January 1991/1992, northern high-latitude MLS and NMC temperatures differed by more than 20 K, and MLS $\chi^2$ were often 4 times larger than typical values. OHP, located at 44°N, is the northernmost lidar in this intercomparison and provides an independent measurement during these times. Validation studies of the CNRS lidar stations [*Keckhut et al.*, 1993] at Centre d'Essai des Landes, Biscarosse (CEL), OHP, and the ship *H. Poincaré*, comparing with radar-tracked radiosondes, rocket-released falling spheres, and the LIMS data [*Remsberg*, 1986] show differences less than 3.5 K from 37 to 64 km and less than 1 K between 30 and 35 km. Figure 22 shows lidar, MLS, and NMC profiles on 6, 10, 27, December 1991, and 3 January 1992. The closest MLS profiles are 260, 110, 160, and 390 km away from the lidar, and were measured within 1, 1, 162, and 4 min of the midpoint of the lidar integration. The MLS $\chi^2$ for these profiles are 147, 134, 188, and 158, and are typical for Version 3. The NMC profiles are obtained using the same interpolation method outlined before and are analyzed for 1200 UT (although the TOVS profiles were collected at 1500 UT). Since the lidar and MLS measurements are taken close to 0000 UT, Sun-synchronized atmospheric disturbances should be represented similarly in the MLS and CNRS data sets but not in the NMC. The smoothed lidar profile tracks the MLS profile, and both place the stratopause at the same height and with similar lapse rates, except 27 December, when MLS places the stratopause ≈ 5 km (log-pressure coordinates) above the lidar. The 27 December coincidence has the largest time and latitude differences (the MLS profile is located at 42.6°N) of all four comparisons and suggests that differences with lidar temperatures may be dominated by atmospheric variability. Coincidences are usually poorer than 1° in latitude and 3 hours in time, and the 15 K temperature difference (at 2 hPa) is probably indicative of temporal or spatial variability

**Table 6.** Lidar Stations Used in Intercomparison

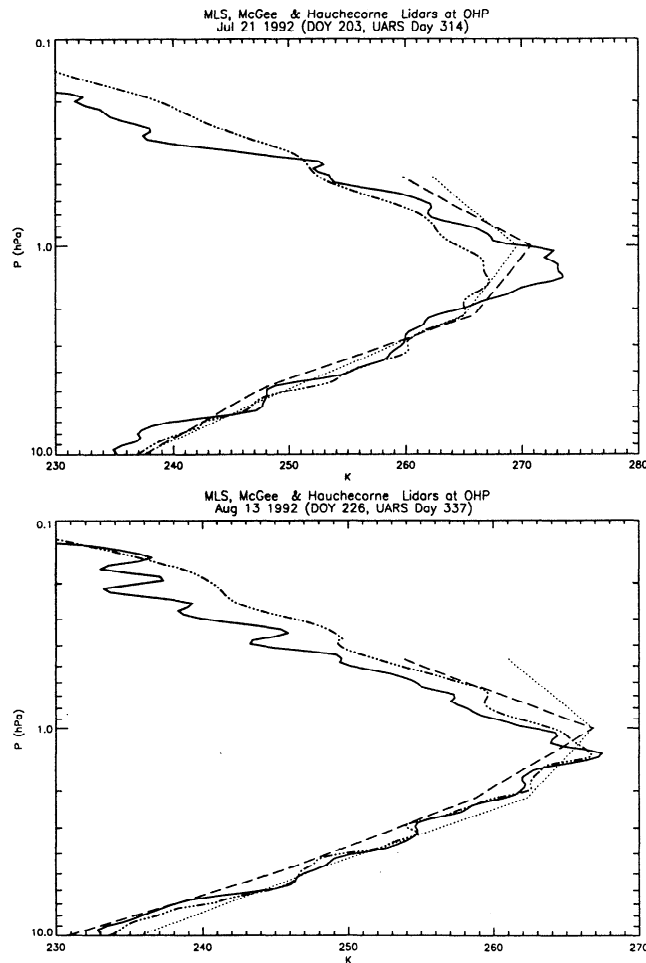| Station | Latitude | Longitude | Number of Profiles (Integration Time, hours) | |
| | | | Permanent Station | Mobile Station |
|---|---|---|---|---|
| TMF | 34° N | 241 ° E | 147 (2) | 18 (4–5) |
| GSFC | 39° N | 283 ° E | | 16 (4–5) |
| OHP | 44° N | 6 ° E | 95 (1) | 20 (3–4) |
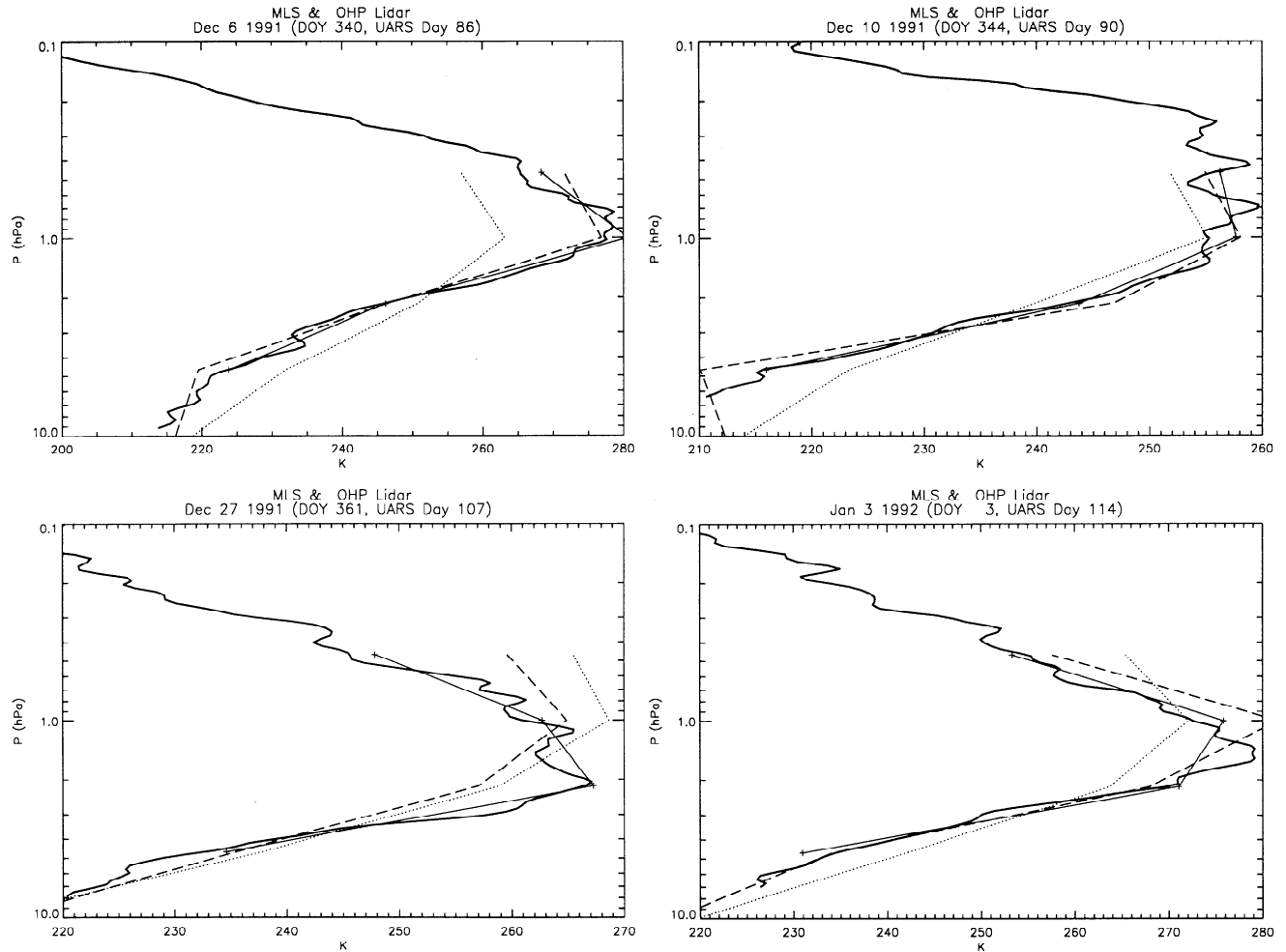
**Figure 22.** Comparison of lidar profiles from the Centre National de la Recherche Scientifique (CNRS) lidar at Observatory of Haute-Provence (OHP) (44° N, 6° E) and closest MLS profiles during winter 1991/1992 on 6 December, 10 December, 27 December and 3 January. The lidar measurements were collected around 0002, 2241, 1943, and 0225 UT, while the MLS measurements were collected at 0004, 2241, 1701, and 0225 UT. The MLS measurements were located at 43.1° N, 9.1° E (265 km away), 43.7° N, 4.7° E (110 km), 42.6° N, 6.6° E (164 km), and 45° N, 10.7° E (391 km). The original unsmoothed lidar profile is shown by the thick solid line and its projection on the MLS vertical grid by the thin solid line with plus signs. The MLS profile is shown by the dashed line and the NMC profile at 1200 UT is shown by the dotted line.

in the comparison. Differences arising from spatial and temporal variability are expected to be unbiased and average to zero in the limit of large sample size. We estimate that with 100 profile comparisons, systematic differences larger than 1–2 K can be estimated. The lowest level in the smoothed lidar profile is 4.6 hPa, and both the smoothed lidar and the MLS temperatures are consistently cooler than NMC, which are measured during the afternoon. MLS measures the same location twice daily approximately 12 hours apart. On each of these day the afternoon profile at 1225 UT, 1100 UT, 1700 UT, and 1405 UT were 2 K, 2 K, 6.5 K, and 0.5 K warmer than the morning profiles at 4.6 hPa. Assuming that these differences provide an estimate of diurnal variability at OHP, only a fraction of the cold bias in the NMC temperatures can be explained by diurnal variability. Although winter high-latitude lidar data

are sparse, the available data suggest that large high-latitude winter MLS–NMC differences are not indicative of lower accuracy in MLS temperatures.

Figure 23 shows profiles from the lidar intercomparisons at OHP on 21 July and 13 August 1992. The two lidar use different wavelengths and are operated simultaneously, but the integration time for the CNRS lidar measurements was 1 hour in comparison with 3–4 hours for STROZ-LITE. STROZ-LITE was also located at TMF for a similar lidar intercomparison in February and March 1992. The lidar operated sequentially, with the JPL lidar and STROZ-LITE typically integrating for 2 hours and 5 hours, respectively. Figure 24 shows profile comparisons on 26 February and 19 March 1992. Generally, STROZ-LITE shows less vertical wave structure than either the JPL or the CNRS lidars. Gravity waves are believed to generate
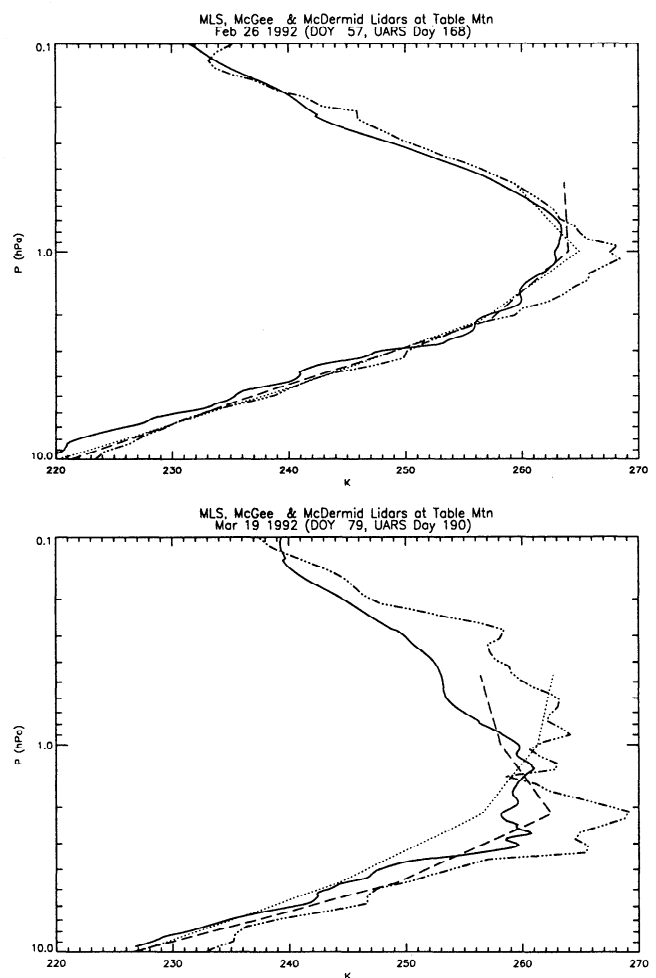
**MLS, McGee & Hauchecorne Lidars at OHP**
**Jul 21 1992 (DOY 203, UARS Day 314)**



**MLS, McGee & Hauchecorne Lidars at OHP**
**Aug 13 1992 (DOY 226, UARS Day 337)**

**Figure 23.** Comparison between lidar profiles and MLS profiles during summer 1992 when Statospheric Ozone Lidar Trailer Experiment (STROZ-LITE) was located at OHP (44° N, 6° E) on 21 July and 13 August. The STROZ-LITE profile is shown as the thick solid line, the CNRS lidar by the dashed-triple dotted line, the MLS profile by the dashed line, and the NMC profile by the dotted line. The CNRS lidar operated around 2113 (20 July) and 0030 UT, while the STROZ-LITE lidar operated at 0125 and at 0141 UT. The MLS profiles are at 43.1° N, 3.8° E, 2034 UT (20 July, 202 km away), and at 45.1° N, 6.8° E, 0030 UT (140 km away).

profiles should remove differences arising from gravity waves in the upper stratosphere and mesosphere, differences between MLS and the smoothed lidar profiles of 5 K are probably indicative of atmospheric variability if the measurements are several hours apart.

Structures in profiles that evolve over longer time-scales, such as the sharpness of the stratopause (i.e., curvature of the profile) is seen in the MLS data at both lidar sites. For example, the sharp stratopause seen in the lidar profile at OHP on 13 August is captured somewhat in the MLS profile, although the lowering of the stratopause from 1 hPa on 21 July to 1.5 hPa is not seen because of the MLS vertical resolution. MLS also observes the broader stratopause at TMF but overestimates the width of the stratopause on 26 February.



**MLS, McGee & McDermid Lidars at Table Mtn**
**Feb 26 1992 (DOY 57, UARS Day 168)**



**MLS, McGee & McDermid Lidars at Table Mtn**
**Mar 19 1992 (DOY 79, UARS Day 190)**

most of this structure, and with estimated periods of 4 hours and 8 km, vertical wavelengths near 50 km altitude [*Chanin and Hauchecorne*, 1981] should be attenuated in the STROZ-LITE data because of its longer integration time and absent in MLS because of its poorer vertical resolution. Differences in temperature at the stratopause at TMF on both days and at OHP on 21 July have both long and short vertical scales, whereas the differences at OHP on 13 August have only short vertical scales. The lidars operated within 1.2 hours on 13 August, while on the other days, they operated approximately 4 hours, apart. The absences of long vertical scales in the differences on 13 August possibly arises because tides are similarly represented in both data sets. In summary, while smoothing of the lidar

**Figure 24.** Comparison with lidar profiles at Table Mountain Facility (TMF) during late winter 1992 on 26 February and 19 March during STROZ-LITE, Jet Propulsion Laboratory (JPL) intercomparison campaign at TMF. The line styles are the same as Figure 23 except that the dash-triple dotted line refers to the profile from the JPL lidar. The STROZ-LITE measurements were collected around 0838 and 1051 UT while the JPL lidar collected its measurements at 0445 and 0703 UT. The MLS profiles are at 35.2° N, 242.2° E, 0528 UT (95 km away), and 34.6° N, 244.6° E, 0901 UT (212 km away).

Temperature MLS(Solid Line) Table Mtn Lidar(★)
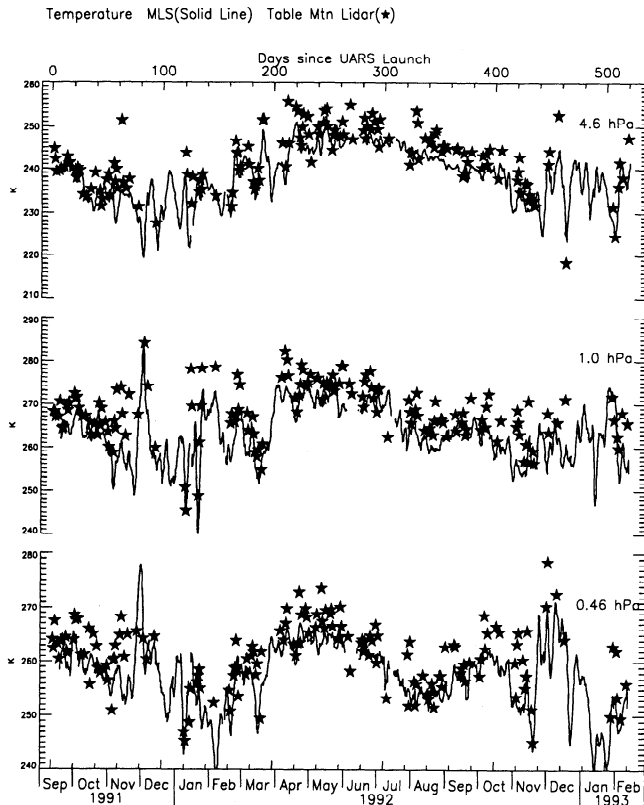


**Figure 25.** Time series of MLS (line) and TMF lidar (stars) temperatures at 4.6 hPa, 1 hPa, and 0.46 hPa, during the first 520 days of MLS operation. The MLS curve shows all days when MLS collected data. On days when the JPL lidar was not operating, the local time of the bracketing JPL profiles was interpolated to the day of the MLS measurements, and the closest profile within 12 h of that time was used.

A possible explanation is that MLS is losing sensitivity near 0.46 hPa. In contrast, NMC profiles (also shown in Figures 23 and 24) do not successfully represent either broad or narrow stratopauses.
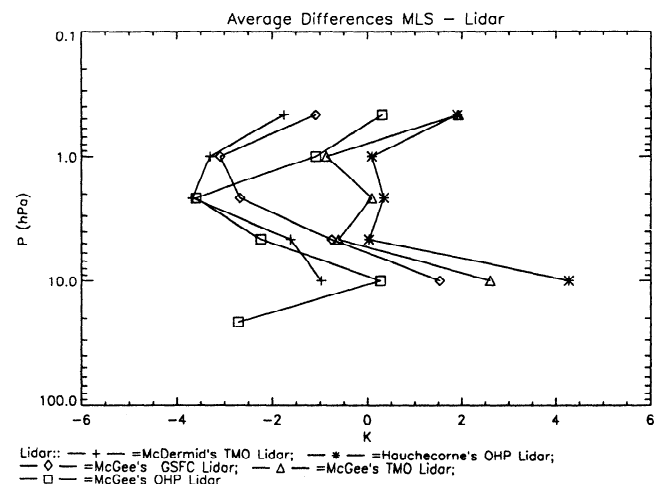
Even though MLS and lidar profiles show large differences arising from rapid, small-scale features, longer-term trends, such as the annual cycle, are similarly represented in both data sets. The JPL lidar collected 147 near-coincident profiles with MLS during the first 520 days of MLS operation. Figure 25 shows the time series of MLS and smoothed TMF temperatures at 4.6, 1, and 0.46 hPa. During the winter, both data sets capture sudden warming events, although the lidar shows larger fluctuations. With this exception, there is no evidence that MLS temperatures during the winter are in less agreement with TMF temperatures than other seasons.

Mean biases between MLS and lidar temperatures are summarized in Figure 26. The total number of profiles for each station used in these comparisons is listed in Table 6; STROZ-LITE profiles are separated by location of measurement (GSFC, TMF, and OHP). The STROZ-LITE comparisons have fewer profiles, typically 10–20, as compared with the CNRS and JPL lidars which had 95 and 147 profiles, and statistical noise fluc-

tuations (mostly atmospheric) from the smaller sample sizes are expected to be 2-3 times larger. The TMF and STROZ-LITE data are generally warmer than MLS by approximately 1-4 K between 4.6 hPa and 1 hPa. MLS is warmer than the CNRS lidar but by less than 0.5 K. Differences with the three STROZ-LITE data sets vary between 0 K and -2 K. In comparisons with MLS the CNRS lidar is warmer than the JPL lidar, but the STROZ-LITE lidar at OHP is colder than the STROZ-LITE lidar at TMF. This suggests that mean STROZ-LITE – MLS temperature differences are site dependent because of the small sample size. At 10 hPa the CNRS lidar shows a 4 K cold bias which is approximately twice as large as the STROZ-LITE bias. The CNRS lidar at 10 hPa may be biased cold by Pinatubo aerosols and STROZ-LITE with its Raman channel probably provides the the more accurate data set. In comparisons with LIMS temperatures between 43 and 46 km ($\approx$ 2 hPa) the CNRS lidar at OHP was found to be 0.5 K colder during May 1979 and approximately 1–2 K colder during April [*Remsberg*, 1986]. The JPL lidar shows a warm bias compared to MLS and the other lidar. In comparisons between STROZ-LITE (without the Raman channel) and the JPL lidar during the 1989 Stratosphere Ozone Intercomparison Campaign (STOIC), the JPL lidar was also observed to be 2 K warmer than STROZ-LITE at 30 km [*Ferrare et al.*, 1995].

## 7. Summary of Estimated Errors

The analysis of section 3 has shown that the current MLS retrieval algorithms have sensitivity to atmospheric temperature between 22 hPa and 0.46 hPa. Precision, accuracy, and stability have been estimated and are tabulated in Table 3. Precision has contributions associated with measurement noise (less than 0.5 K) and scan-dependent forward model interpolation



Lidar:: — + — =McDermid's TMO Lidar; — ✳ — =Hauchecorne's OHP Lidar;
— ◊ — =McGee's GSFC Lidar; — △ — =McGee's TMO Lidar;
— □ — =McGee's OHP Lidar

**Figure 26.** Average differences between the closest MLS profile and the JPL lidar at TMF (pluses), the CNRS lidar at OHP (asterisks), STROZ-LITE at Goddard Spaceflight Center (diamonds), STROZ-LITE at TMF (triangles), and STROZ-LITE at OHP (squares).

errors (around 1 K). Accuracy is thought to be limited primarily by errors in the $O_2$ line-broadening parameter and forward model errors and varies between 3 K and 5.3 K. Most of the error in line broadening parameter is manifested as a 1.5– 2.2 K cold bias, and although this is presented as a separate column in the table, it is also included in the accuracy estimate. The biases listed in Table 3 should be subtracted from MLS Version 3 temperatures. The accuracy of these corrected temperatures is the root difference between the squares of the accuracy and bias. MLS temperatures have the poorest stability at the period of a yaw cycle (72 days, and atmospheric trends with this period may have instrumental artifacts around 0.15–0.35 K in amplitude. Stability over longer timescales, or over an orbit, is better than 0.1 K.

Comparisons with other data sets confirm the estimated biases. MLS temperatures are lower than NMC and lidar temperatures (except CNRS) by 1–2 K in the stratosphere, as expected from an error in $O_2$ line-broadening parameter. A yaw-period synchronized oscillation in MLS – NMC differences is 10 times larger than explained by instrumental effects and is believed to be caused primarily by atmospheric tides. Differences in MLS and TOVS vertical resolution are identified in comparisons of temperature near the stratopause and can produce MLS – NMC temperature differences larger than 5 K that are spatially and seasonally correlated. MLS Version 3 temperatures are lower than NMC in the middle and upper stratosphere at high latitudes during the winter, and profiles from the CNRS lidar agree better with MLS than NMC. With the estimated bias added, MLS temperatures tend to lie within the spread of lidar measurements; the JPL lidar is 1 to 2 K warmer than MLS, the CNRS lidar is 1 to 2 K cooler than MLS, and STROZ-LITE differs from MLS by 1 K warmer or cooler, depending on the altitude. Temperature differences between MLS and lidar profiles are often around 10 K especially at the stratopause and oscillate with height; most of the oscillation (5 K amplitude) is associated with gravity waves [*Wilson et al.*, 1991]. Upper stratospheric and mesospheric temperature differences between near-coincident MLS and lidar profiles seem to be related to time differences between measurements, and can be 2 K for 2 hours differences. These differences are believed to be related to tides.

Tangent-point pressure is retrieved from 10 to 0.046 hPa and its errors are summarized in Table 4. Tangent-point pressure precision is better than 100 m and is as small as 10 m at 0.46 hPa. Estimated biases in tangent-point pressure, derived from biases in the $O_2$ line-broadening parameters, vary between 200 m and 340 m ( <6%) and account for most of the estimated accuracy. The accuracy of corrected tangent-point pressures is estimated to be approximately equal to the measurement precision.

## 8. Topics for Future Work

Future development of the MLS processing software is expected to reduce some of the error sources discussed

here. Version 4 files will use updated $O_2$ line-broadening parameters, eliminating the biases listed in Table 3 and new sideband ratios derived from radiance residuals. A major component in temperature inaccuracy arises from radiometric gain inaccuracy. Temperature errors from radiometric gain inaccuracy are strongly correlated between pressure levels and a more complete study of the correlation should allow the temperature inaccuracy at all levels to be specified by a single parameter. This reformulated accuracy is particularly important to the lapse rate, which should have better accuracy than would be estimated if the accuracies are uncorrelated.

Improvements in the calculation of radiance are expected to increase the vertical extent of useful temperatures and tangent-point pressures. With an improved Zeeman line-splitting correction, channels 7, 8, and 9 will provide additional information above 0.46 hPa. Improvements in the numerical accuracy of the forward model are expected to allow the retrieval of useful temperatures at 46 hPa, and the improved closure should eliminate the forward model error covariance $E_f$ in the error covariance.

Changes in the retrieval algorithms to more effectively use altitude differences from the antenna-pointing encoder are planned and will more accurately tie the tangent-point pressure and temperature retrievals together through hydrostatic balance. This will extend the useful range of measurements and increase the precision of temperature and tangent-point pressure throughout the retrieval range.

Figure 27 shows the improved precision and accuracy that can be expected. Temperature precision with improved algorithms should be better than 0.3 K from 46 hPa to 1 hPa and tangent-point pressure precision should be better than 20 m between 20 hPa and 0.05 hPa. Temperature accuracy should be better than 2.5 K between 46 hPa and 0.46 hPa, and should be strongly cross correlated. Tangent-point pressure accuracy should be
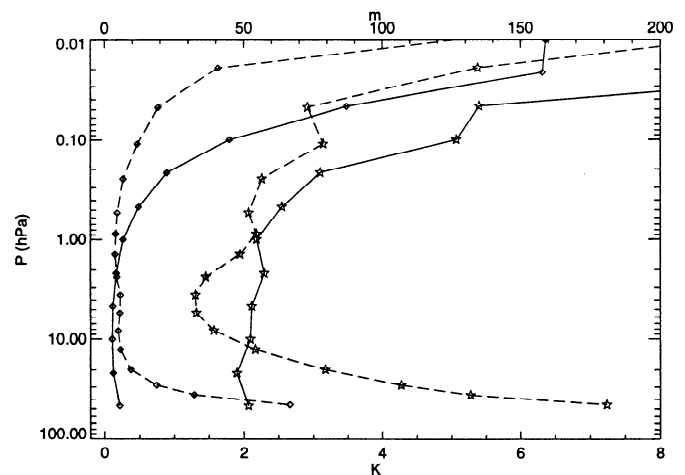


**Figure 27.** Accuracy (stars) and precision (diamonds) expected from improved algorithms, instrument characterization, and spectroscopic parameters. The solid lines are the curves for temperature and are plotted against the scale on the bottom, and the dashed lines are for tangent-point pressure and are plotted against the scale at the top.

better than 80 m between 20 hPa and 0.1 hPa. Temperature accuracy will improve by a factor of 2 (from 4.6 K at 1 hPa to around 2 K) and tangent-point pressure accuracy should improve by a factor greater than 25.

# References

Andrews, D. G., J. R. Holton, and C. B. Levoy, *Middle Atmosphere Dynamics*, 489pp., Academic Press, Orlando, Flor., 1987.

Barath, F. T., et al., The upper atmosphere research satellite microwave limb sounder instrument, *J. Geophys. Res., 98*, 10,751–10,762, 1993.

Barraclough, D. R., International Geomagnetic Reference Field: The fourth generation, *Phys. Earth Planet. Inter., 48*, 279-292, 1987.

Canziani, P. O., J. R. Holton, E. F. Fishbein, L. Froidevaux, and J. W. Waters, Equatorial Kelvin waves: A UARS MLS view, *J. Atmos. Sci., 51*, 3053 3076, 1994.

Chanin, M.-L., and A. Hauchecorne, Lidar observations of gravity and tidal waves in the stratopause and mesosphere, *J. Geophys. Res., 86*, 9715–9721, 1981.

Ferrare, R. A., T. J. McGee, D. Whiteman, J. Burris, M. Owens, J. Butler, R. A. Barnes, F. Schmidlin, W. Komhyr, P. H. Wang, M. P. McCormick, and A. J. Miller, Lidar measurements of stratospheric temperature during STOIC, *J. Geophys. Res., 100*, 9303 9312, 1995.

Finger, F. G., H. M. Woolf, and C. E. Anderson, A method for objective analysis of stratospheric constant-pressure charts, *Mon. Weather Rev., 93*, 619–638, 1965.

Finger, F. G., M. E. Gelman, J. D. Wild, M. L. Chanin, A. Hauchecorne, and A. J. Miller, Evaluation of NMC upper stratospheric temperature analyses using rocketsondes and lidar data, *Bull. Am. Meteorol. Soc., 74*, 789–799, 1993.

Fishbein, E. F., L. S. Elson, L. Froidevaux, G. L. Manney, W. G. Read, J. W. Waters, and R. W. Zurek, MLS observations of stratospheric waves in temperature and $O_3$ during the 1992 southern winter, *Geophys. Res. Lett., 20*, 1255–1258, 1993.

Fleming, E. L., S. Chandra, M.R. Schoeberl, and J.J. Barnett, Monthly mean global climatology of temperature, wind, geopotential height and pressure from 0–120 km, *NASA Tech. Memo., 100697*, 85+v pp., 1988.

Froidevaux, L., et al., Validation of UARS microwave limb sounder ozone measurements, *J. Geophys. Res.*, this issue.

Gelman, M. E., and R. M. Nagatani, Objective analysis of height and temperature at the 5-, 2-, and 0.4-mb levels using meteorological rocketsondes and satellite radiation data, *Space Res., XVII*, 117–122, 1977.

Gelman, M. E., A. J. Miller, K. W. Johnson, and R. M. Nagatani, Detection of long-term trends in global stratospheric temperature from NMC analyses derived from NOAA satellite data, *Adv. Space Res., , 6R*, 17–26, 1986.

Gelman, M. E., A. J. Miller, R. M. Nagatani, and H. D. Bowman III, Use of UARS data in the NOAA stratospheric monitoring program, *Adv. Space Res., 14*, 21–31, 1994.

Grody, N. C., Remote sensing of the atmosphere from satellites using microwave radiometry, in *Atmospheric Remote Sensing by Microwave Radiometry*, edited by M. A. Janssen, pp. 259–311, John Wiley, New York, 1993.

Jarnot, R. F., R. E. Cofield, J. W. Waters, G. E. Peckham and D. A. Flower, Calibration of the Microwave Limb Sounder on the Upper Atmosphere Research Satellite, *J. Geophys. Res.*, this issue.

Keckhut, P., A. Hauchecorne, and M. L. Chanin, A critical review of the database acquired for the long-term surveillance of the middle atmosphere by the French Rayleigh lidars, *J. Atmos. Oceanic Technol., , 10*, 850–867, 1993.

Keckhut, P., et al., Temperature measurements intercomparison at OHP using Rayleigh lidar and UARS instruments, *Proc. 17th Intl. Laser Radar Conf.*, 510-511, Sendai, Japan, 1994.

Lahoz, W. A., et al., Validation of UARS Microwave Limb Sounder 183 GHz $H_2O$ measurements, *J. Geophys. Res.*, this iss

Liebe, H. J., G. A. Hufford, and R. O. DeBolt, it The Atmospheric 60 GHz Oxygen Spectrum: Modeling and laboratory measurements, NTIA-Rep. 91-272, U.S. Dep. of Commerce, Boulder, Colo., 1991.

Liebe, H. J., P. W. Rosenkranz, and G. A. Hufford, Atmospheric 60-GHz oxygen spectrum: New laboratory measurements and line parameters, *J. Quant. Spectrosc. Radiat. Transfer, 48*, 629–643, 1992.

Massie, S. T., P. L. Bailey, J. C. Gille, E. C. Lee, J. T. Mergenthaler, A. E. Roche, J. B. Kumer, E. F. Fishbein, J. W. Waters, and W. A. Lahoz, Spectral signatures of polar stratospheric clouds and sulfate aerosols, *J. Atmos. Sci., 51*, 3027–3044, 1994.

McDermid, I. S., S. M. Godin, and T. D. Walsh, Lidar measurements of stratospheric ozone and intercomparisons and validation, *Appl. Opt., 29*, 4914–4923, 1990.

McGee, T. J., M. R. Gross, U. N. Singh, J. J. Butler, and P. E. Kimvilakani, Improved stratospheric ozone lidar, *Opt. Eng., 34*, 1421–1430, 1995.

Papoulis, A., *Probability, Random Variables, and Stochastic Processes*, 583+xi pp., McGraw-Hill, New York, 1965.

Pickett, H. M., R. L. Poynter, and E. A. Cohen, Submillimeter, millimeter and microwave spectral line catalog, Tech. Rep. 80-23, revision 3, Jet Propul. Lab., Pasadena, Calif., 1992.

Poynter, R. L., and H. M. Pickett, Submillimeter, millimeter and microwave spectral line catalog, *Appl. Opt., 24*, 2235–2240, 1985.

Randel, W. J., J. C. Gille, A. E. Roche, J. B. Kumer, J. L. Mergenthaler, J. W. Waters, E. F. Fishbein, and W. A. Lahoz, Stratospheric transport from the tropics to middle latitudes by planetary-wave mixing, *Nature , 365*, 533–535, 1993.

Ray, E. A., J. R. Holton, E. F. Fishbein, L. Froidevaux, and J. W. Waters, The tropical semi-annual oscillation in temperature and ozone as observed by the MLS, *J. Atmos. Sci., 51*, 3045–3052, 1994.

Reber, C. A., The Upper Atmospheric Research Satellite (UARS), *Geophys. Res. Lett., 20*, 1215–1218, 1993.

Remsberg, E. E., The accuracy of Nimbus 7 LIMS temperature in the mesosphere, *Geophys. Res. Lett., 13*, 311–314, 1986.

Remsberg, E. E., P. P. Bhatt, and T. Miles, A comparison of Nimbus 7 Limb Infrared Monitor of the Stratosphere and radiosonde temperatures in the lower stratosphere poleward of 60° N, *J. Geophys. Res.*, *97*, 13,001–13,014, 1992.

Remsberg, E. E., P. P. Bhatt, and F. J. Schmidlin, Time series comparisons of satellite and rocketsonde temperatures in 1978-79, *NASA Tech. Pap.*, *3409*, 137 pp., 1994.

Rodgers, C. D., Retrieval of atmospheric temperature and composition from remote measurements of thermal radiation, *Rev. Geophys.*, *14*, 609–624, 1976.

Rodgers, C. D., Characterization and error analysis of profiles retrieved from remote sounding measurements, *J. Geophys. Res.*, *95*, 5587–5595, 1990.

Rosenkranz, P. W., Interference coefficients for overlapping oxygen lines in air, *J. Quant. Spectrosc. Radiat. Transfer*, *39*, 287–297, 1988.

Rosenkranz, P. W,. and D. H. Staelin, Polarized thermal microwave emission from oxygen in the mesosphere, *Radio Sci.*, *23*, 721–729, 1988.

Schmidlin, F. J., Intercomparisons of temperature, density and wind measurements from in situ and satellite techniques, *Adv. Space. Res.*, *4*, 101–110, 1984.

Smith, W. L., H. M. Woolf, C. M. Hayden, D. Q. Wark, and L. M. McMillin, The TIROS-N operational vertical sounder, *Bull. Am. Meteorol. Soc.*, *60*, 1177–1187, 1979.

Waters, J. W., K. F. Kunzi, R. L. Pettyjohn, R. K. L. Poon, and D. H. Staelin, Remote sensing of atmospheric temperature profiles with the Nimbus 5 microwave spectrometer, *J. Atmos. Sci.*, *32*, 1953–1969, 1975.

Waters, J. W., et al., Validation of UARS Microwave Limb Sounder ClO measurements, *J. Geophys. Res.*, this issue.

Wild, J. D, et al., Comparisons of statospheric temperatures from several lidars using National Meteorological Center and Microwave Limb Sounder data as transfer references, *J. Geophys. Res.*, *100*, 11,105-11,111, 1995.

Wilson, R., M. L. Chanin, and A. Hauchecorne, Gravity waves in the middle atmosphere observed by Rayleigh lidar, 1, Case studies, *J. Geophys. Res.*, *96*, 5153–5167, 1991.

E.F. Fishbein, R.E. Cofield, L. Froidevaux, R.F. Jarnot, T. Lungu, W.G. Read, Z. Shippony, J.W. Waters, I.S. McDermid, Jet Propulsion Laboratory, California Institute of Technology, Pasadena, California.

T.J. McGee NASA Goddard Spaceflight Center, Greenbelt, Maryland.

U. Singh, M. Gross, Huges STX Corporation, Lanham, Maryland.

A. Hauchecorne, P. Keckhut, Service d'Aeronomie du Centre National de la Recherche Scientifique, Verrieres le Buisson, France.

M.E. Gelman, R.M. Nagatani, Climate Prediction Center, National Centers for Environmental Protection, National Weather Service, NOAA, Camp Springs, Maryland.